



HAL
open science

DART : a 3D model for remote sensing images and radiative budget of earth surfaces

Jean-Philippe Gastellu-Etchegorry, Eloi Grau, Nicolas Lauret

► **To cite this version:**

Jean-Philippe Gastellu-Etchegorry, Eloi Grau, Nicolas Lauret. DART : a 3D model for remote sensing images and radiative budget of earth surfaces. Modeling and simulation in Engineering, 2012, pp.ISBN 978-953-307-959-2. ird-00658284

HAL Id: ird-00658284

<https://ird.hal.science/ird-00658284>

Submitted on 10 Jan 2012

HAL is a multi-disciplinary open access archive for the deposit and dissemination of scientific research documents, whether they are published or not. The documents may come from teaching and research institutions in France or abroad, or from public or private research centers.

L'archive ouverte pluridisciplinaire **HAL**, est destinée au dépôt et à la diffusion de documents scientifiques de niveau recherche, publiés ou non, émanant des établissements d'enseignement et de recherche français ou étrangers, des laboratoires publics ou privés.

Chapter Number

DART: A 3D Model for Remote Sensing Images and Radiative Budget of Earth Surfaces

J.P. Gastellu-Etchegorry, E. Grau and N. Lauret
CESBIO - CNES, CNRS (UMR 5126), IRD, Université de Toulouse, Toulouse, France

1. Introduction

Knowledge of the radiative behavior and the energy budget of land surfaces is essential for studying the functioning of natural and urban surfaces with remotely acquired information. Account of their 3D nature is often essential because in most cases these surfaces are not isotropic. For example, it has long been known that the albedo of a canopy with an anisotropic Bi-directional Reflectance Factors (BRF) may be underestimated by as much as 45% if it is computed with nadir reflectance only (Kimes and Sellers, 1985). Radiative transfer (R.T.) models have the potential for correcting this type of error provided they account for the three dimensional (3D) nature of Earth surfaces. Neglect of the 3D structure of canopies can lead to large errors on the 3D radiation budget and remote sensing measurements. For example, for vegetation BRF and directional brightness temperature (DTDF) distribution functions, errors can be as large as 50%, depending on instrumental (*e.g.*, view and sun directions) and experimental (*e.g.*, vegetation heterogeneity) conditions (Gastellu-Etchegorry *et al.*, 1999). The problem is similar for urban canopies due to their strong spatial heterogeneity. The application of R.T. modeling to urban surfaces is important in the context of the advent of satellite sensors with spatial and spectral resolutions that are more and more adapted to urban characteristics such as building dimensions and temperature spatial variability. It explains the numerous works conducted in the field of remote sensing of urban surfaces (Soux *et al.*, 2004; Voogt and Oke, 1998). The use of descriptions with qualitatively based land use data instead of more fundamental surface descriptors is a source of inaccuracy for modeling BRFs and DTDFs (Voogt and Oke, 2003).

R.T. models are essential tools for assessing accurately radiative quantities such as the exitance, the irradiance and remote sensing measurements in the optical and thermal domains. However, in order to meet this objective, models must account for the three dimensional (3D) nature of Earth surfaces. Here, we consider vegetation canopies and urban canopies. This consideration of the 3D architecture of Earth surfaces is possible with the so-called 3D models. Generally speaking, the latter ones are intended to be accurate, robust and more comprehensive than other models. Ideally, they should be used in place of other models. However, they are often more difficult to manage, both in terms of computation

1 time and landscape description. Moreover, when dealing with specific situations, one needs
2 that the model be accurate and robust, but one does not necessarily need that the model be
3 comprehensive. This explains that in many cases, the objective of 3D models is to calibrate
4 models that are simpler to manage in terms of landscape description, computation time, etc.
5 Once calibrated, these models can meet the required accuracy levels.

6 These remarks stress the usefulness of 3D R.T. models. A number of 3D models is being
7 developed by the scientific community (Widlowski *et al.*, 2007). Usually, they are designed
8 for a given type of landscape (*e.g.*, natural or urban), with or without topography and
9 atmosphere, for a specific type of application (*e.g.*, remote sensing or radiation budget), and
10 for a given spatial resolution of analysis (*e.g.*, simulation of a tree crown with or without
11 branches). Moreover, remote sensing models are usually designed for a given spectral
12 domain (*e.g.*, sun reflected spectral domain or thermal infrared spectral domain).

13 A common problem when designing a R.T. model is to assess to which level of detail
14 landscapes must be taken into account. This is very especially important in term of
15 landscape simulation. However, it affects also the mathematical formulation of R.T.
16 Generally speaking, one should take into account all landscape elements that have a
17 significant influence on the application we are dealing with (*i.e.*, landscape radiative budget
18 or remote sensing measurement). In practice, the answer can be complex. For example,
19 when simulating remote sensing measurements of heterogeneous Earth surfaces in the
20 visible spectral domain, is it necessary to simulate the atmosphere within a unique "Earth -
21 Atmosphere" system in order to simulate with a good accuracy its complex interaction with
22 earth surfaces?

23 Some of these aspects are discussed here with the brief presentation of DART (Discrete
24 Anisotropic Radiative Transfer) model. This is one of the most complete 3D models
25 designed for simulating the radiative budget and the satellite observations of the land
26 surfaces in the visible, near infrared and thermal infrared of land surfaces. It was originally
27 developed (Gastellu-Etchegorry *et al.*, 1996) for simulating remote sensing images of 3D
28 vegetation canopies in the visible / near infrared (NIR) spectral domain. Afterwards, it was
29 extended to the thermal infrared domain and to the simulation of any landscape: urban or
30 natural, with atmosphere and topography. As a result, the present DART model simulates
31 the radiation budget and remote sensing images of vegetation and urban canopies, for any
32 experimental (sun direction, canopy heterogeneity, topography, atmosphere, etc.) and
33 instrumental (view direction, spatial resolution, etc.) configuration.

34 After a brief presentation of DART, two types of applications are discussed: urban and
35 forest canopies. This is followed by the presentation of three recent improvements:

- 36 - Account of the Earth / Atmosphere curvature for oblique remote sensing
37 measurements.
- 38 - Possibility to import 3D objects simulated as the juxtaposition of triangles and to
39 transform them into 3D turbid objects.
- 40 - Possibility to simulate landscapes that have a continuous topography and landscapes
41 that are non repetitive.

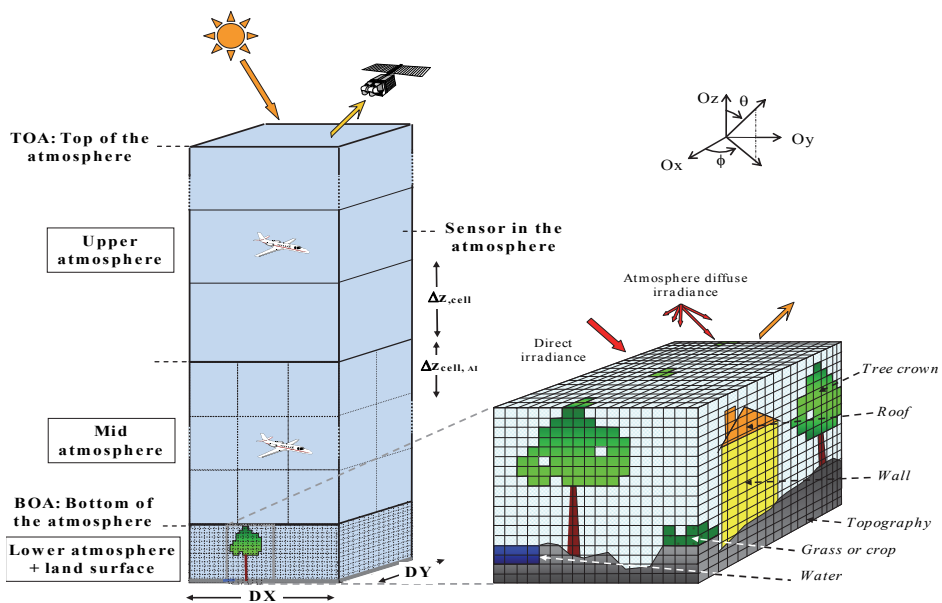
42 Finally, preliminary results concerning two application domains are discussed. 1) 2D
43 distributions of reflectance, brightness temperature and radiance of the African continent
44 that would be measured by a geostationary satellite. 2) Radiative budget of urban (Gastellu-
45 Etchegorry, 2008) and natural (Belot, 2007) canopies. They are simulated with a DART
46 energy budget (EB) component, called DARTEB, under development.

2. DART model

1 DART was originally developed for simulating BRFs (Bi-directional Reflectance Factor),
 2 remote sensing images and the spectral radiation budget of 3D natural (*e.g.*, trees, roads,
 3 grass, soil, water) landscapes in the visible and short wave infrared domains. Since its first
 4 release in 1996, it was successfully tested, in the case of vegetation canopies, against
 5 reflectance measurements (Gastellu-Etchegorry *et al.*, 1999) and against a number of 3-D
 6 reflectance models (*e.g.*, *Flight* (North, 1996), *Sprint* (Thompson and Goel, 1998), *Raytran*
 7 (Govaerts and Verstraete, 1998)), in the context of the RAMI (Radiation transfer Model
 8 Intercomparison) experiment (Pinty *et al.*, 2001; Pinty *et al.*, 2004; Widlowski *et al.*, 2007;
 9 Widlowski *et al.*, 2008). Only BRFs could be compared because DART was the only 3-D
 10 model that simulates images.

11 DART was successfully used in many scientific domains: impact of canopy structure on
 12 satellite images texture (Pinel and Gastellu-Etchegorry, 1998) and reflectance (Gastellu-
 13 Etchegorry *et al.*, 1999), 3D distribution of photosynthesis and primary production rates of
 14 vegetation canopies (Guillevic and Gastellu-Etchegorry, 1999), influence of Norway forest
 15 spruce structure and woody elements on LAI retrieval (Malenovsky *et al.*, 2005) and canopy
 16 reflectance (Malenovsky *et al.*, 2008), determination of a new hyperspectral index for
 17 chlorophyll estimation of forest canopy (Malenovsky *et al.*, 2006), study of tropical forest
 18 texture (Barbier *et al.*, 2010; Barbier *et al.*, 2011; Proisy C. *et al.*, 2011).

19 DART simulates R.T. in heterogeneous 3-D landscapes with the exact kernel and discrete
 20 ordinate methods. It uses an iterative approach: radiation intercepted in iteration "i" is
 21 scattered in iteration "i+1". Any landscape is simulated as a rectangular matrix of
 22 parallelepipedic cells. Figure 1 illustrates the way urban and natural landscapes are
 23
 24



25
 26 Fig. 1. DART cell matrix of the Earth / Atmosphere system.
 27 The atmosphere has 3 levels: upper (*i.e.*, layers with any depth), mid (*i.e.*, cells with any size)

1 and lower (*i.e.*, cells identical to land surface cells) atmosphere. Land surface elements are
 2 the juxtaposition of triangles and/or turbid cells.

3 simulated, possibly with topography and atmosphere. The atmosphere is made of cells the
 4 size of which increases with altitude. Radiation is restricted to propagate in a finite number
 5 of directions (Ω_i) with an angular sector width ($\Delta\Omega_i$) (sr). Any set of N discrete directions can
 6 be selected ($\sum_{n=1}^N \Delta\Omega_n = 4\pi$). A radiation that propagates along direction (Ω_i) at a position r
 7 is called a source vector $W(r, \Omega_i)$. It has 3 components: total radiation W, radiation unrelated
 8 to leaf mesophyll and polarization degree associated to first order scattering.

9 DART can work in 3 operating modes: flux tracking, Lidar and Monte Carlo. Only, the flux
 10 tracking mode is considered here. This mode tracks emitted and scattered radiation fluxes
 11 (*i.e.*, watts) within angular cones. The Monte Carlo mode tracks individual photons that are
 12 emitted by the sun or a sensor. It is a reference tool for testing the accuracy of the flux
 13 tracking mode. The Lidar mode uses the Monte Carlo mode and keeps track of the path
 14 length (*i.e.*, time) of each single photon.

15 For the flux tracking mode, there are 3 sub modes:

- 16 - Mode reflectance (R): sun is the only source of radiation. Atmosphere is a secondary
 17 source.
- 18 - Mode temperature (T): the atmosphere and the land surfaces are the sources of
 19 radiation. They depend on temperature and wavelength, using either the Planck's law
 20 or the Boltzmann law. Boltzmann law is especially useful for simulation radiation
 21 budget over the whole spectrum.
- 22 - Mode (R + T): the sun, atmosphere and land surfaces are the radiation sources. This
 23 mode is very useful for simulating remote sensing measurements in the 3-4 μ m spectral
 24 domain.

25 For the 3 modes, the atmosphere can be treated as a propagating medium or as an interface.
 26 In any case, landscape irradiance has 2 components: direct sun $W(\Omega_s, x, y)$ and atmospheric
 27 $W_a(\Omega_n, x, y)$ source vectors. $W(\Omega_s)$ propagates along direction (Ω_s). $W(\Omega_s)$ and $W_a(\Omega_n)$ are
 28 simulated from a fictitious cell layer on top of the scene (Figure 1), with values equal to:

$$29 \quad W(\Omega_s) = E_s(\Omega_s) \cdot |\mu_s| \cdot \Delta x \cdot \Delta y \quad \text{and} \quad W_a(\Omega_n) = L_a(\Omega_n) \cdot |\mu_n| \cdot \Delta x \cdot \Delta y \cdot \Delta\Omega_n$$

30 where $\Delta x \cdot \Delta y$ is the area of the cell face, $\mu_s = \cos\theta_s$, $\mu_n = \cos\theta_n$, $E_s(\Omega_s)$ is the solar constant at the
 31 top of the scene, and Ω_s denotes the solar incident direction. $L_a(\Omega_n)$ is the atmospheric
 32 radiance along direction (Ω_n), with $n \in [1 \dots N']$, where N' is the number of downward discrete
 33 directions. It is null at the top of the atmosphere.

34 DART landscape modeling is as independent as possible from the RT modeling in order to
 35 allow DART to simulate RT on landscapes simulations that are generated by any other
 36 model. It can combine them with its own simulated landscapes. Imported landscapes and
 37 landscape elements can be edited to some extent. Geometric transformations (*i.e.*, 3D
 38 translation, 3D homothety, 3D rotation) can be applied and optical properties can be
 39 assigned.

40 DART uses 2 complementary approaches for simulating landscapes:

- 41 - Juxtaposition of cells that contain one or several turbid medium (*i.e.*, cloud of infinitely
 42 small planar elements). This is useful for simulating volumes of foliar elements such as
 43 grass and tree crown. A turbid medium is characterized by its volume density, an
 44 angular distribution and optical properties (*i.e.*, abaxial reflectance, adaxial reflectance,
 45 transmittance).

1 - Juxtaposition of translucent triangles. This is useful for simulating the ground, the
 2 branches, the urban surfaces (*i.e.*, walls and roofs) and also foliar elements. A single cell
 3 can contain several turbid medium and several triangles or part of them.

4 In addition to the atmosphere and to the ground and its topography, DART simulates 4
 5 types of landscape elements:

6 - Trees with exact or random locations and specific optical properties. Each tree is made
 7 of a trunk, possibly with branches, simulated as triangles, and a tree crown simulated as
 8 the juxtaposition of turbid cells. Tree crown can have a number of predefined shapes
 9 (*e.g.*, ellipsoid, cone, trapezoid, etc.), with specific vertical and horizontal distributions
 10 of leaf volume density. Trees with different geometric and optical properties can be
 11 mixed.

12 - Grass or crops. They are simulated as a volume of turbid medium. This volume can
 13 be located anywhere in space (x,y,z).

14 - Urban elements (*i.e.*, houses, roads,...). The basic element is a house with walls
 15 characterized by the location of their 4 upper corners and roofs characterized by their 4
 16 upper corners.

17 - Water elements (*i.e.*, river, lake). They are simulated as surfaces with any optical
 18 property (*e.g.*, anisotropic reflectance possibly with specular component).

19 Generally speaking, two types of radiation interaction take place. (1) Volume interaction
 20 within turbid cells (Gastellu-Etchegorry *et al.*, 2004). (2) Surface interaction on triangles
 21 (Gastellu-Etchegorry, 2008). First scattering order is exactly computed in turbid cells, using 2
 22 points on the ray path within the cell: one point for upward scattering and one point for
 23 downward scattering. As expected, simplifying hypotheses are used for simulating multiple
 24 scattering in turbid cells. Its computation uses a much faster method than the initial
 25 "harmonic expansion" method: it uses the energy intercepted within a finite number of
 26 incident angular sectors $\Omega_{\text{sect},k}$ that sample the 4π space of directions ($\sum \Omega_{\text{sect},k} = 4\pi$). An
 27 angular sector Ω_{sect} is a set of close discrete directions. Their number can be as large as the
 28 number of directions of ray propagation, but a number equal to 6 leads to very accurate
 29 results, with relative errors smaller than 10^{-3} (Gastellu-Etchegorry *et al.*, 2004). Actually,
 30 these points are computed for each sub-face of each cell face f ($f \in [1 \ 6]$) that intercepts
 31 incident rays, and for each angular sector "incident" on the cell face (Martin, 2006; Grau,
 32 2011). This implies that intercepted vector sources $W_{\text{int}}(s,f,\Omega_{\text{sect},k})$ are stored per sub face s of
 33 cell face f and per incident angular sector $\Omega_{\text{sect},k}$. Thus, we have:
 34 $W_{\text{int}}(s,f,\Omega_{\text{sect},k}) = \sum \Omega_s W_{\text{int}}(s,f,\Omega_s)$, with directions (Ω_s) within ($\Omega_{\text{sect},k}$). For the case "direct sun
 35 illumination", there is 1 sector only.

36 Atmospheric R.T. modeling is implemented for any spectral band in the optical domain
 37 from the ultraviolet up to the thermal infrared (Gascon, 2001; Grau and Gastellu-Etchegorry,
 38 2011). It simulates the atmospheric backscattering phenomenon, which avoids the need to
 39 couple DART with an atmospheric model. Atmospheric optical properties are characterized
 40 by the molecular $P_m(\lambda,\Omega,\Omega)$ and aerosol $P_p(\lambda,\Omega,\Omega)$ phase functions and by a number of
 41 profiles (molecular extinction coefficient $\alpha_e^m(\lambda,z)$ and spherical albedo $\omega_m(\lambda,z)$, aerosol
 42 extinction coefficient $\alpha_e^p(\lambda,z)$ and spherical albedo $\omega_p(\lambda,z)$). These quantities are specified by
 43 the operator or come from a data base ([0.3 μm 30 μm]) pre-computed with the Modtran
 44 atmospheric model (Berk *et al.*, 1989), for a few predefined atmospheres. DART TOA (Top
 45 Of the Atmosphere) reflectance, transmittance and brightness temperature values are very
 46 close to Modtran simulations for any atmosphere, any BOA (Bottom Of the Atmosphere)
 47 surface and sun / view configuration (Grau, 2011).

Several tools are integrated in the DART model for facilitating the task of the users. Major tools are listed below:

- Sequencer of simulations: it runs a set of simulations where a predefined number of DART input variables vary. For example, one can run $A_1^{N_1} \cdot A_2^{N_2} \cdot A_3^{N_3} \cdot A_4^{N_4} \dots$ simulations where DART input variables A_1, A_2, A_3, \dots take N_1, N_2, N_3, \dots , respectively. Results are stored in a LUT (Look Up Table) for further display and / or processing.
- Manipulation of DEM (Digital Elevation Model): this is used for importing, creating and resampling DEMs.
- Simulation of foliar spectra with the Prospect model (Jacquemoud and Baret, 1990).
- Simulation of scene spectra (reflectance, brightness temperature, radiance). It can be computed using a single DART simulation that is conducted with N spectral bands, or with the help of the sequencer for running N DART simulations with 1 spectral band each.
- Simulation of broadband reflectance, brightness temperature, radiance, irradiance, ... It is the sum of a few DART simulated narrow spectral bands, possibly weighted by sensor spectral sensitivity.
- Importation of land cover maps for a direct simulation of DART scenes.

DART models and tools are managed with a user friendly Graphic User Interface (GUI: Figure 2) to input all necessary parameters (e.g., view and illumination conditions) and to specify the required products. They can be also managed with command lines such as scripts written in Python programming language. DART computation code is written in C++ language (more than 300 000 lines of code). The GUI is written in Java language.

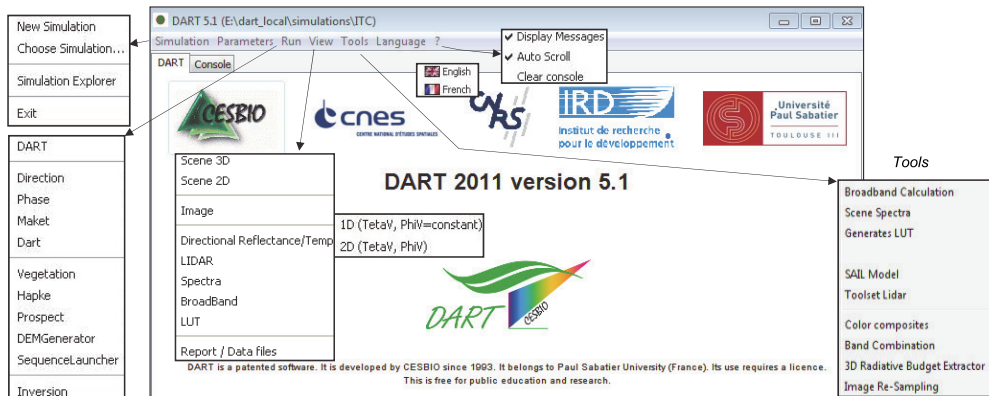


Fig. 2. Graphic User Interface of DART.

'Simulation': creation of simulation folders. 'Parameters': input of DART parameters. 'Run': simulation of scene and RT. 'View': display of results. 'Tools': for deriving products from DART simulations.

DART provides two major types of products:

- Remote sensing measurements at 3 altitude levels: BOA, TOA and atmosphere level. Measurements are essentially images for the "Flux tracking" mode and waveforms for the "Lidar" mode. Images are simulated in the focal plane of the satellite sensor. The cross section of the emitters and scatterers at the origin of the signal are taken into

1 account for improving the image quality, especially for scenes with marked 3D
2 architectures (urban elements, topography). A bi-linear interpolation method is used for
3 projecting the horizontal upper grid of the scene onto an over sampled grid in the
4 sensor plane, at any altitude (BOA to TOA).
5 - Radiative budget: 3D, 2D and 1D distribution of the radiation that is intercepted,
6 scattered, emitted and absorbed.

7 **3. Examples of DART simulations**

8 DART potential for simulating remote sensing images of urban and forest canopies is
9 illustrated here with 2 examples.

10 **3.1 Urban canopy**

11 The example shown here is derived from the CAPITOUL project of Meteo France (Masson
12 *et al.*, 2007) that took place over the city of Toulouse, France, from February 2004 to
13 February 2005. Study of urban energy balance was one of the objectives. For that, different
14 types of measurements took place: acquisition of TIR airborne images, in-situ
15 measurements of turbulent fluxes, surface energy balance, surface temperatures, etc.
16 DART was used for simulating remote sensing images and the radiative budget (Gastellu-
17 Etchegorry, 2008). First, we developed a specific program for creating a DART scene from
18 the urban database (Autocad format) and digital elevation model (DEM) of the Toulouse
19 town hall (France). This led to the creation of DART objects (*e.g.*, houses, trees). The fact
20 that urban elements in the data base are not individual houses or buildings but unrelated
21 walls and roofs was a difficulty. Figure 3 shows nadir (a) and oblique (b) color composites
22 of the St Sernin district of Toulouse city. They were created with DART simulations in the
23 blue, green and red spectral bands. Simulations stress that urban reflectance and
24 brightness temperature values display a marked angular heterogeneity. This
25 heterogeneity is illustrated here with the angular distribution of NIR reflectance values of
26 St Sernin district (*Figure 4*).

27 Figure 3.c and d display DART remote sensing images of St Sernin basilica, in the center of
28 district. They are simulated for a sensor at the bottom of the atmosphere (*i.e.*, BOA image)
29 and for a sensor at the top the atmosphere (TOA). The bluish tone of the TOA image,
30 compared to the BOA image, is due to the fact that atmosphere scatters more in the blue
31 than in the red spectral domain. DART images realism is very useful for verifying that the
32 land surface is correctly simulated. Moreover, it helps also for testing the coherence of the
33 RT. For example, at the 1st scattering order, the reflectance of shadows is null.

34 **3.2 Forests**

35 One considers here DART simulations of the reflectance of a tropical forest (Sumatra,
36 Indonesia) in the visible (VIS), near infrared (NIR) and short wave infrared (SWIR) spectral
37 domains. Optical and geometric characteristics are given in Gastellu-Etchegorry *et al.*, 1998.
38 Sun direction is characterized by a 35° off-nadir angle (θ_s) and a 200° azimuth angle (ϕ_s).
39 Figure 5 shows DART VIS images for three viewing directions: nadir viewing direction
40 ($\theta_v=0^\circ$), sun backscattering viewing direction ($\theta_v=35^\circ$, $\phi_v=200^\circ$), also called hot spot
41 configuration, and specular configuration ($\theta_v=35^\circ$, $\phi_v=20^\circ$).



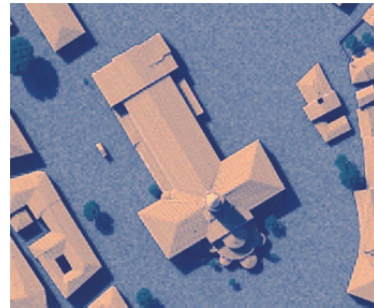
a)



b)

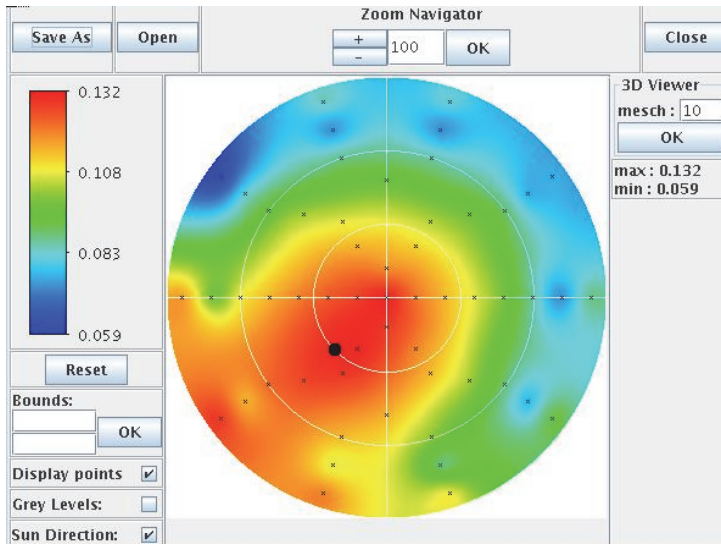


c)

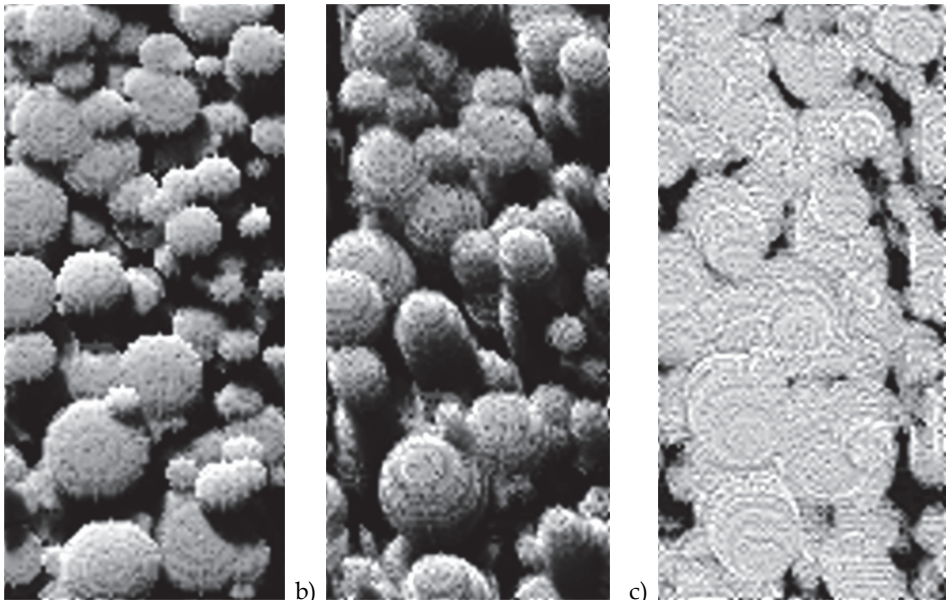


d)

Fig. 3. DART simulated nadir (a) and oblique (b) images of St Sernin district. They are color composites made with blue, green and red DART simulated images. c) Zoom of black box in a); St Sernin basilica. d) Top of the atmosphere simulation.



1
2 Fig. 4. Example of near infrared BRF of St Sernin district.
3 It is computed with simulated reflectance values (crosses), for a sun direction shown by a
4 black circle. Distance from the circle centre gives the view zenith angle ($[0\ 90^\circ]$) and the anti
5 clockwise angle from the horizontal axis gives the azimuth view angle ($[0\ 360^\circ]$).
6



7
8 Fig. 5. VIS DART images of tropical forest (Sumatra, Indonesia). Sun direction: $\theta_s=35^\circ$,
9 $\phi_s=200^\circ$. (a) Nadir ($\rho \approx 0.031$), (b) specular ($\theta_v=35^\circ$, $\phi_v=20^\circ$: $\rho \approx 0.023$), and (c) hot spot ($\rho \approx 0.091$)
viewing directions. SKYL=0.

- 1 - Nadir viewing direction (Figure 5.a). Mean canopy reflectance is ($\rho_{\text{vis}} \approx 0.031$, $\rho_{\text{nir}} \approx 0.376$,
 2 $\rho_{\text{swir}} \approx 0.143$). Illuminated and shaded tree crowns have very different reflectances,
 3 shown here with gray tones. Only trees of the upper canopy are easily distinguished.
 4 Surfaces with a reflectance smaller than 0.02, *i.e.* shaded crowns and understory,
 5 represent 36% of the total scene area. Reflectance of illuminated crown is $\rho_{\text{vis}} \approx 0.048$
 6 ($\rho_{\text{nir}} \approx 0.55$, $\rho_{\text{swir}} \approx 0.21$).
- 7 - Specular direction (Figure 5.b), *i.e.* ($\theta_v = 35^\circ$, $\phi_v = 20^\circ$). Mean canopy reflectance is
 8 ($\rho_{\text{vis}} \approx 0.023$, $\rho_{\text{nir}} \approx 0.344$, $\rho_{\text{swir}} \approx 0.119$). The reflectance difference between nadir and
 9 specular directions stresses the non lambertian nature of forest BRDF. Vertical sides of
 10 tree crowns can be observed, which explains why trees appear with larger dimensions,
 11 compared to nadir viewing direction. This forward scattering configuration is mainly
 12 characterized by the important proportion of dark shadows, *i.e.* light trapping, due to
 13 the 3-D distribution of trees. Surfaces with a reflectance smaller than 0.02, *i.e.* shaded
 14 crowns and understory, occupy 50% of the total scene area. Reflectance of illuminated
 15 crown is ($\rho_{\text{vis}} \approx 0.037$, $\rho_{\text{nir}} \approx 0.51$, $\rho_{\text{swir}} \approx 0.18$). Thus, crown VIS, NIR and SWIR reflectance is
 16 smaller than in the nadir configuration. This is explained by the fact the sunlit crown
 17 fraction and the leaf scattering phase function $\frac{1}{4\pi} P(\Omega_s, \Omega_v)$ are smaller.
- 18 - hot spot configuration (Figure 5.c), *i.e.* ($\theta_v = 35^\circ$, $\phi_v = 200^\circ$). The absence of shade in this
 19 configuration explains the strong canopy reflectance in all spectral domains, *i.e.*
 20 $\rho_{\text{vis}} \approx 0.091$ ($\rho_{\text{nir}} \approx 0.684$, $\rho_{\text{swir}} \approx 0.341$). Darkest areas correspond to the low reflecting
 21 understory. Their reflectance is less than 0.03 and occupy about 5% of the total scene
 22 area. Crown reflectance is ($\rho_{\text{vis}} \approx 0.1$, $\rho_{\text{nir}} \approx 0.74$, $\rho_{\text{swir}} \approx 0.4$).

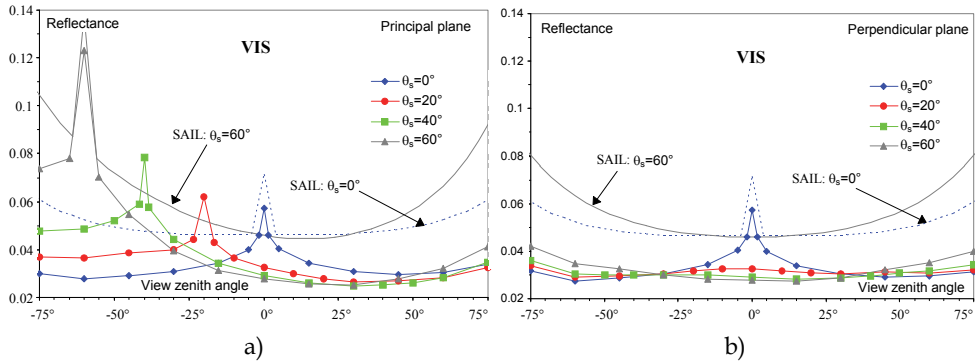
23 Figure 6 shows DART NDVI (Normalized Vegetation Index) and VIS / NIR / SWIR
 24 reflectance values in the principal and perpendicular solar planes, for several sun off-nadir
 25 directions. Reflectance values share some similar characteristics: (1) a well marked bowl
 26 shape in the principal solar plane with a spectrally dependent minimum for a direction
 27 between the specular and nadir directions, (2) a strong maximum in the hot spot direction,
 28 more marked in the VIS than in the NIR and SWIR, (3) a systematic increase of reflectance if
 29 view zenith angles exceed a threshold value (*e.g.* $\approx 50^\circ$ in the VIS if $\theta_s = 0^\circ$), which depends on
 30 the spectral domain and the sun direction, (4) an azimuth symmetry relative to the principal
 31 solar plane, and (5) a relatively small variability in the perpendicular solar plane.

32 Reflectance is maximal at hot spot ($\rho_{\text{vis}} = 0.073$, $\rho_{\text{nir}} = 0.615$, $\rho_{\text{swir}} = 0.324$) and minimal for
 33 directions between nadir and specular configurations ($\rho_{\text{vis}} = 0.025$, $\rho_{\text{nir}} = 0.354$, $\rho_{\text{swir}} = 0.12$),
 34 whereas NDVI is minimal (≈ 0.79) in the hot spot direction and maximal (≈ 0.87) in the
 35 specular direction.

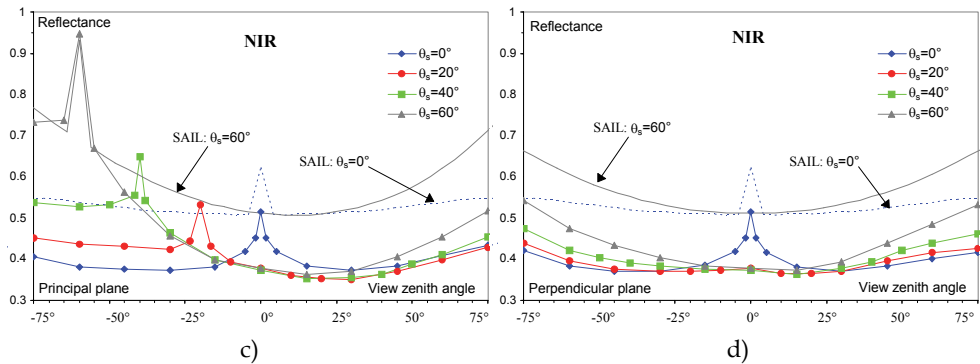
36 In addition to DART simulations, Figure 6 shows reflectance simulations carried out with
 37 the well known SAIL model (Verhoef, 1984). For this model, vegetation is an homogeneous
 38 turbid medium. Figure 6 allows one to stress the role of canopy architecture on forest
 39 reflectance. Its neglect by the SAIL model explains that DART reflectance is much smaller.
 40 Reflectance differences depend a lot on view direction. Smaller differences occur in the hot
 41 spot directions because no shadows occur for these viewing directions. Outside the hot spot
 42 configuration, for $\theta_s = 0^\circ$, mean relative reflectance difference is around 60-70% in the VIS,
 43 50% in the SWIR and 25% in the NIR. Differences tend to increase with sun off-nadir angle.

44 The bowl shape of VIS and SWIR reflectance is more marked with SAIL than with DART. It
 45 corresponds to the fact that in the forward principal plane, for large off-nadir viewing
 46 angles θ_v , an increase of θ_v implies that DART reflectance increases less than SAIL

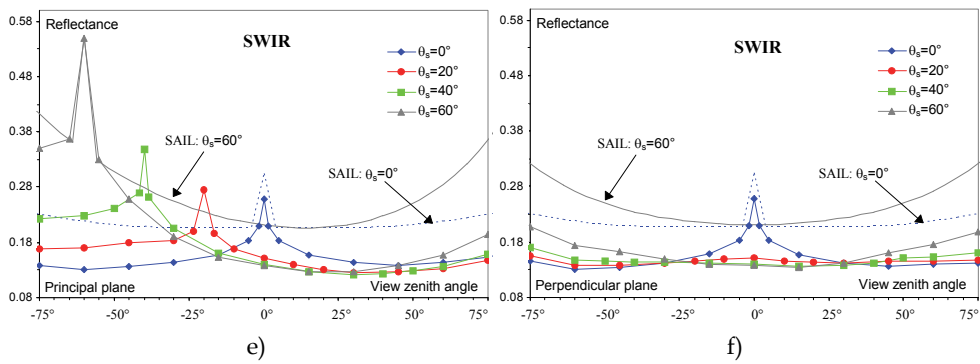
1 reflectance, especially for large off-nadir sun angles. Indeed, the canopy 3-D heterogeneous
 2 structure ensures that an increase of θ_v leads to an increase of the proportion of shaded tree
 3 crowns that are viewed in the principal plane. This effect tends to be less marked in the NIR
 4 than in the VIS because the role of shadows is less marked in the NIR, due to the increased
 5 occurrence of multiple scattering processes. Moreover, the presence of shadows explains
 6 that with oblique sun illumination, minimal values of DART reflectance are more shifted
 7 towards the specular direction than those of SAIL. This is also true for NDVI.
 8



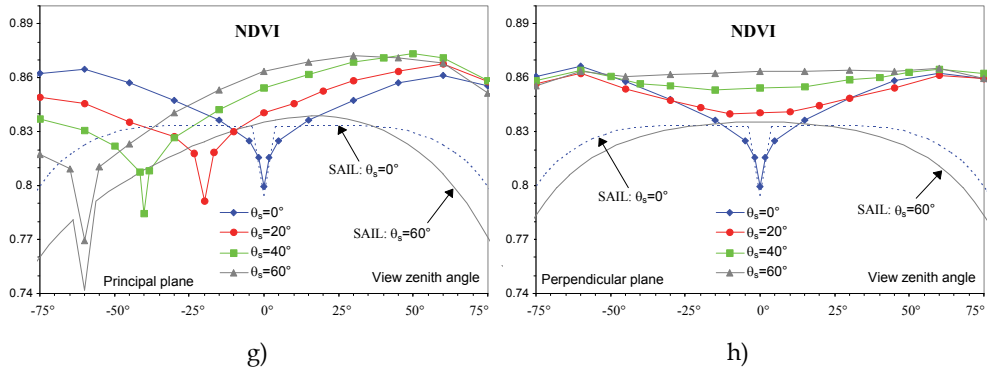
9
10
11



12
13
14



15
16



1

2

3 Fig. 6. Tropical forest angular DART and SAIL VIS (a, b), NIR (c, d), SWIR (e, f) simulated
 4 reflectance and NDVI (g, h) for 4 sun off-nadir directions (0° , 20° , 40° , 60°). Principal
 5 (left column) and perpendicular (right column) solar planes. SKYL is 0.3 for VIS, 0.24 for
 6 NIR and 0.09 for SWIR. For a better clarity SAIL simulations are for $\theta_s = 0^\circ$ and 60° only.

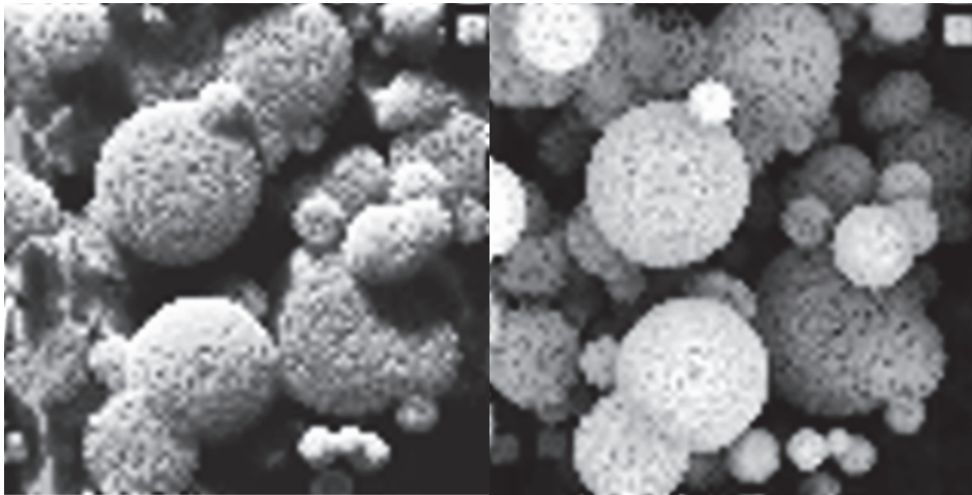
7 Image simulation is very useful for understanding forest reflectance behavior with
 8 experimental and instrumental parameters. Here, this is shown for sky radiation. Figure 7
 9 shows DART nadir NIR images of part of the tropical forest, for 2 extreme atmosphere

10 conditions: SKYL equal to 0 and 1, with $SKYL = \frac{\text{Atmosphere irradiance}}{\text{Total irradiance}}$. We note that some

11 tree crowns are invisible with SKYL=0 (bottom of Figure 7), because they are shaded, and

12

13



14

15

16 Fig. 7. NIR DART nadir images of a tropical forest with SKYL equal to 0 (a) and 1 (b). Most
 17 crowns of upper trees that are shaded with SKYL=0 are well lit if SKYL=1. Moreover,
 18 shaded crowns of a few lower trees that are not viewed with SKYL=0 become visible if
 19 SKYL=1. Sun off-nadir angle is 35° .

1 visible with SKYL=1. It explains that forest reflectance varies with atmosphere radiation. In
2 a first approximation, we can consider that forest reflectance depends on the fraction of
3 illuminated crowns, shaded crowns of upper trees, and shaded lower trees and understory
4 (*i.e.* vegetation smaller than 10m height). With SKYL=0 (SKYL=1), fractions of these 3 classes
5 are around 48% (68%), 37% (12%) and 15% (20%), respectively, whereas their apparent NIR
6 reflectances are around 0.55 (0.52), 0.27 (0.14) and 0.069 (0.062), respectively. As expected, a
7 SKYL increase implies that the area of illuminated crowns increases whereas their apparent
8 reflectance slightly decreases. Indeed, with SKYL=1 all upper trees are totally illuminated,
9 conversely to the case SKYL=0. On the other hand, a SKYL increase implies that the fraction
10 and reflectance of shaded upper trees regularly decrease, whereas the area and apparent
11 reflectance of the shaded lower trees and understory remain nearly constant if SKYL<0.5.
12 The fraction and reflectance decrease of the shaded upper tree crowns results from two
13 opposite effects: when SKYL increases some crown surfaces, only slightly shaded if SKYL=0,
14 become darker whereas crown surfaces that are initially totally shaded become better lit.
15 Thus, when SKYL increases, tree crowns that are initially shaded with SKYL=0, can become
16 lit enough to belong to the category "illuminated upper trees".

17 **4. Recent and on going improvements**

18 Three recent improvements of DART are briefly described here:

- 19 - Earth / Atmosphere curvature. It is important when simulating satellite measurements,
20 because the usual assumption that the Earth is a flat surface is less and less valid with
21 more and more oblique view directions.
- 22 - Transformation of 3D objects made of juxtaposed triangles into 3D turbid objects.
- 23 - Finite landscapes and infinite landscapes with a continuous (*i.e.*, not repetitive)
24 topography.
- 25 - Simulation of Lidar waveform.

26 **4.1 Earth / Atmosphere curvature**

27 The Earth / Atmosphere curvature has an impact at 2 levels: (1) the incidence angle of sun
28 and view directions of Earth surfaces, and (2) ray path lengths in the atmosphere. Both
29 effects are now taken into account by DART.

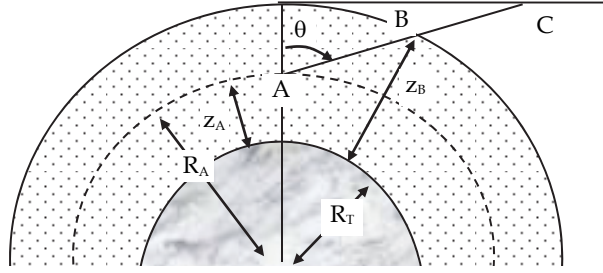
30 View and sun incidence angle

31 For a non-horizontal atmosphere, the incidence angle α differs from the satellite sensor off
32 nadir angle β . DART computes α , β and the azimuth view direction in the Earth surface
33 reference system with the locations (latitude, longitude, altitude) of the Earth target T and
34 satellite sensor S, assuming the Earth to be an ellipsoid (*cf.* Annex).

35 Sun incidence angle at target level and on an horizontal surface below the satellite are
36 computed by DART as a function of time with the equations of the NOAA solar calculator
37 (<http://www.esrl.noaa.gov/gmd/grad/solcalc/>).

38 Ray paths in the atmosphere

39 For an off-nadir angle θ , an atmosphere path length between altitudes z_a and z_b is smaller
40 than in an horizontal atmosphere (*i.e.*, $\Delta z / |\mu|$, with $\mu = \cos\theta$ and $\Delta z = |z_a - z_b|$). Moreover,
41 gas and aerosol vertical distributions are not constant. Here, atmosphere is assumed to be
42 spherical (Figure 27).



R_T : Earth radius,

$R(z)$: radius of the sphere at the altitude z . $R(z) = R_T + z$

θ : zenith angle of a direction ($\mu = \cos\theta$)

1

2 Fig. 8. The atmosphere with the Earth curvature.

3 $\mu = \cos\theta > 0$: Path $\{\Delta z > 0; \mu\}$ is $AB = -R_A \cdot \mu + \sqrt{R_A^2 \cdot \mu^2 + \Delta z \cdot (\Delta z + 2R_A)}$

4 It can be viewed as a path $\{\Delta z; \mu_{sph}\}$ in an horizontal atmosphere if:

5

$$\mu_{sph} = \frac{\Delta z}{-R_A \cdot \mu + \sqrt{R_A^2 \cdot \mu^2 + \Delta z \cdot (\Delta z + 2R_A)}} \Rightarrow AB = \frac{\Delta z}{\mu_{sph}} < \frac{\Delta z}{\mu}$$

6 $\mu = \cos\theta < 0$: Path $\{\Delta z < 0; \mu\}$ is $AB = -R_A \cdot \mu - \sqrt{R_A^2 \cdot \mu^2 + \Delta z \cdot (\Delta z - 2R_A)}$

7 It can be viewed as a path $\{\Delta z; \mu_{sph}\}$ in an horizontal atmosphere if:

8

$$\mu_{sph} = \frac{\Delta z}{R_A \cdot \mu + \sqrt{R_A^2 \cdot \mu^2 + \Delta z \cdot (\Delta z - 2R_A)}} \Rightarrow AB = \frac{-\Delta z}{\mu_{sph}} < \frac{-\Delta z}{\mu}$$

9 Note: the 2 expressions of AB and μ_{sph} are identical. Indeed: $\{\mu > 0, \Delta z > 0\}$ for the 1st one and

10 $\{\mu < 0, \Delta z < 0\}$ for the 2nd one.

11 The optical depth of path AB is:

12 $\Delta \tau(z_A, \Delta z, \mu) = \int_0^{\Delta l = AB} \alpha(t) \cdot dl = \int_{z_A}^{z_B} \alpha(t) \cdot \frac{R_A + t}{\sqrt{R_A^2 \cdot \mu^2 + t \cdot (t + 2R_A)}} \cdot dt$, with t the altitude relative to z_A

13 and 1 the path length from A , we have: $l = -R_A \cdot \mu + \sqrt{R_A^2 \cdot \mu^2 + t \cdot (t + 2R_A)}$ if $\mu > 0$ and :

14 $l = -R_A \cdot \mu - \sqrt{R_A^2 \cdot \mu^2 + t \cdot (t - 2R_A)}$ if $\mu < 0$.

15 The computation of $\Delta \tau(z_A, \Delta z, \mu)$ could be solved with an integration by parts:

16
$$\int_{z_A}^{z_A + \Delta z} \alpha(t) \cdot \frac{R_A + t}{\sqrt{R_A^2 \cdot \mu^2 + t \cdot (t + 2R_A)}} \cdot dt$$

$$= \left[\alpha(t) \cdot (R_A \cdot \mu + \sqrt{R_A^2 \cdot \mu^2 + t \cdot (t + 2R_A)}) \right]_{z_A}^{z_A + \Delta z} - \int_{z_A}^{z_A + \Delta z} \alpha'(t) \cdot \left(-R_A \cdot \mu + \sqrt{R_A^2 \cdot \mu^2 + t \cdot (t + 2R_A)} \right) \cdot dt$$

1 This approach requires the derivative $\alpha'(z)$ of the extinction coefficient. However, $\alpha'(z)$ is
 2 known only for an ideal case such as an exponential atmosphere. In order to work with any
 3 atmosphere (*e.g.*, non exponential vertical profile of O_3), $\Delta\tau(z_a, \Delta z, \mu)$ is computed with:

$$4 \quad \Delta\tau(z_a, \Delta z, \mu) = \overline{\alpha(z)} \cdot AB = \overline{\alpha(z)} \cdot \left| \frac{\Delta z}{\mu_{sph}} \right|, \text{ with } \overline{\alpha(z)} \text{ the mean extinction coefficient within } [z_a$$

5 $z_a + \Delta z]$

6 Thus, before simulating the atmosphere RT, DART computes $\mu_{sph}(z_i, \mu_j)$ for all I atmosphere
 7 layers and all J discrete directions, including the sun direction, with $i \in [1 \ I]$ and $j \in [1 \ J]$.

$$8 \quad \left| \mu_{sph}(z_i, \mu_j) \right| = \frac{\Delta z}{-(R_T + z_i)^2 \cdot |\mu_j| + \sqrt{(R_T + z_i)^2 \cdot \mu_j^2 + |\Delta z| \cdot (|\Delta z| + 2 \cdot (R_T + z_i))}}$$

9 The use of $\mu_{sph}(z_i, \mu_j)$ allows one to treat the atmosphere as an horizontal plane for simulating
 10 the atmosphere RT: any path $\delta r(z_i, \mu_j)$ that is computed for an horizontal atmosphere layer

$$11 \quad [z_i, z_i + Dz] \text{ is replaced by } \delta r_{sph}(z_i, \mu_j) = \delta r(z_i, \mu_j) \cdot \frac{\mu_j(z_i, \mu_j)}{\mu_{sph}(z_i, \mu_j)}.$$

$$12 \quad \text{We have: } \delta r_{sph}(z_i, \mu_j) \leq \delta r_{sph}(z_i, \mu_j) \leq \frac{\Delta z}{\mu_j}$$

13 4.2 Transformation of "3D triangle objects" into "3D turbid objects"

14 As already mentioned DART can import 3D objects (Figure 9) that are simulated as groups
 15 of triangles. In many cases, especially for vegetation, these objects are simulated with
 16 tremendous numbers of triangles (*e.g.*, 10^6 triangles). This is very costly in terms of
 17 computation time and volume memory, especially if we work with forests... In order to
 18 solve this problem, we designed a module that transforms 3D objects simulated as triangles
 19 (*i.e.*, 3D triangle objects) into 3D objects simulated as turbid medium (*i.e.*, 3D turbid objects).
 20 Figure 10 shows the schematic approach. It is reminded that a cell filled with turbid medium
 21 is characterized by its LAI (Leaf Area Index), its leaf angle distribution (LAD) and the leaf
 22 optical properties (*e.g.*, transmittance and adaxial and abaxial reflectance, possibly with
 23 specular parameters). The "transformation" module computes the LAI and LAD of all leaf
 24

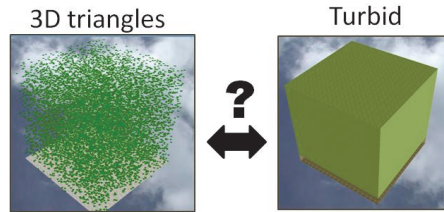


25

26

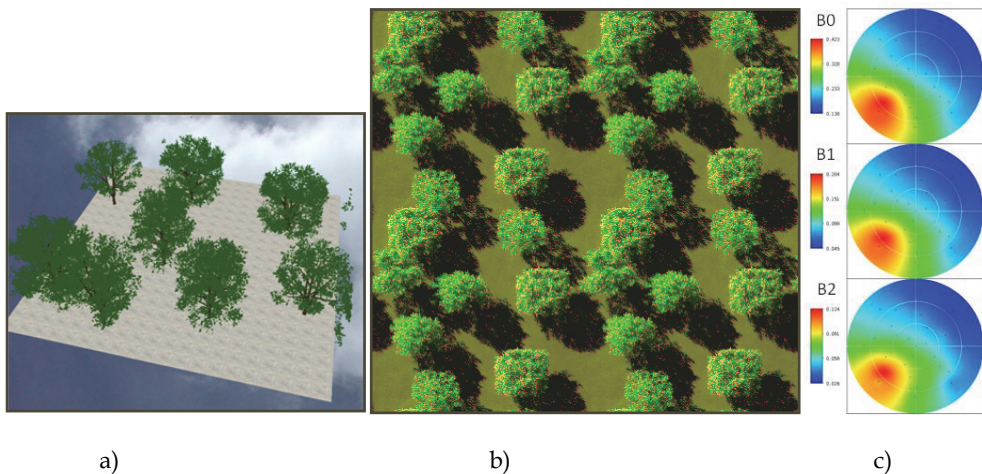
27 Fig. 9. Examples of 3D trees that are imported by DART.

1 elements within each cell of a 3D cell matrix. This is done for all or part of the groups of
 2 triangles of the "3D triangle" object. Optical properties of the turbid medium are those of the
 3 triangles. On the other hand, the LAD is either the one that is computed or a predefined
 4 LAD. The possibility to use a predefined LAD is well adapted to the case of 3D triangle
 5 objects with low volume densities of triangles.
 6

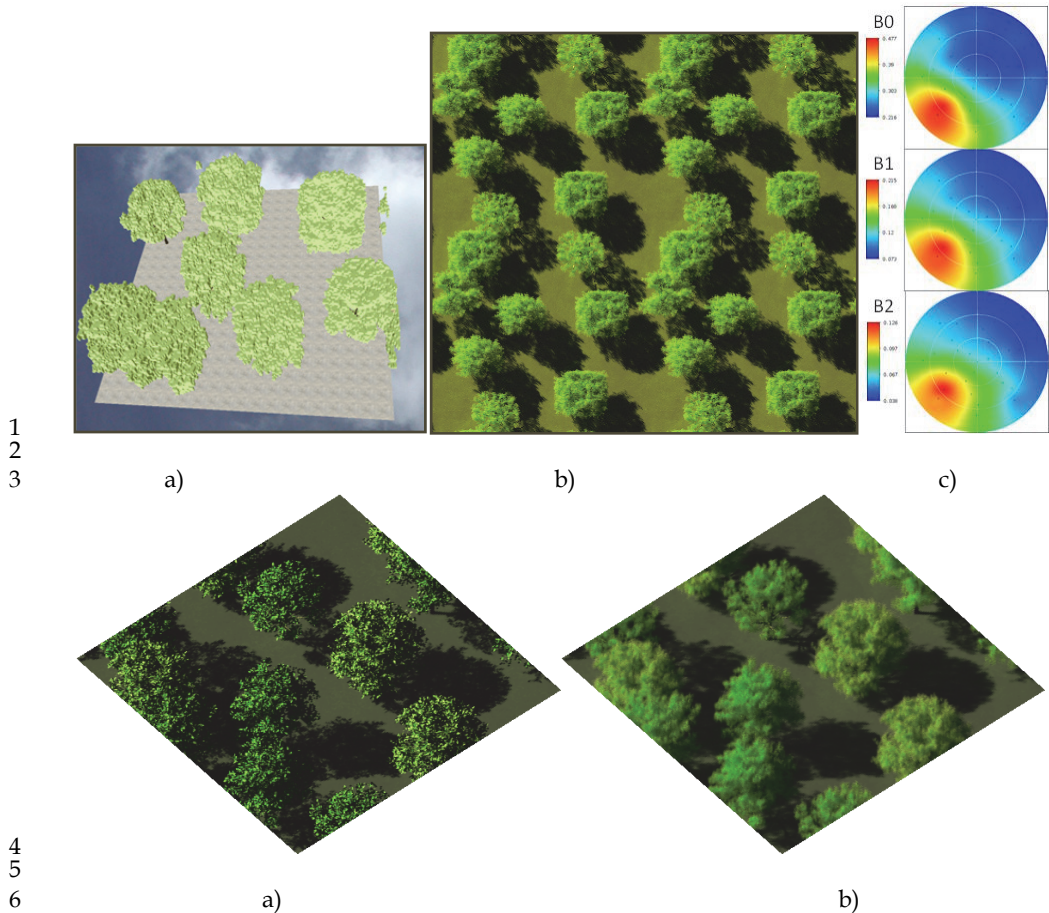


7
 8 Fig. 10. Schematic representation of the transformation of a "triangle cell" into a "turbid
 9 cell".

10 Here, the transformation of a 3D triangle scene into a turbid 3D turbid scene is illustrated by
 11 DART color composite images of the citrus tree "3D triangle scene" and "3D turbid scene"
 12 (Figure 11). The associated 2D reflectance polar plots are shown also. For these
 13 2 cases, RT was simulated in the blue, green and red spectral bands. Results are very
 14 encouraging: reflectance values are very close. Actually, reflectance values of the
 15 3D triangle and turbid scenes are much closer than the 3D triangle objects contain a lot of
 16 triangles. It can be noted that DART images in Figure 11 b and e are duplicated
 17 2 x 2 times. This mode of representation of images is often useful for better interpreting
 18 simulated images where objects (*e.g.*, trees) and their shadows cross the scene boundaries.
 19 Compared to the usual simulation of trees with classical tree crown shapes such ellipsoids
 20 or cones, the transformation of 3D triangle tree crowns into 3D turbid tree crowns is very
 21 interesting for keeping the 3D architecture of trees.
 22
 23
 24



25
 26
 27

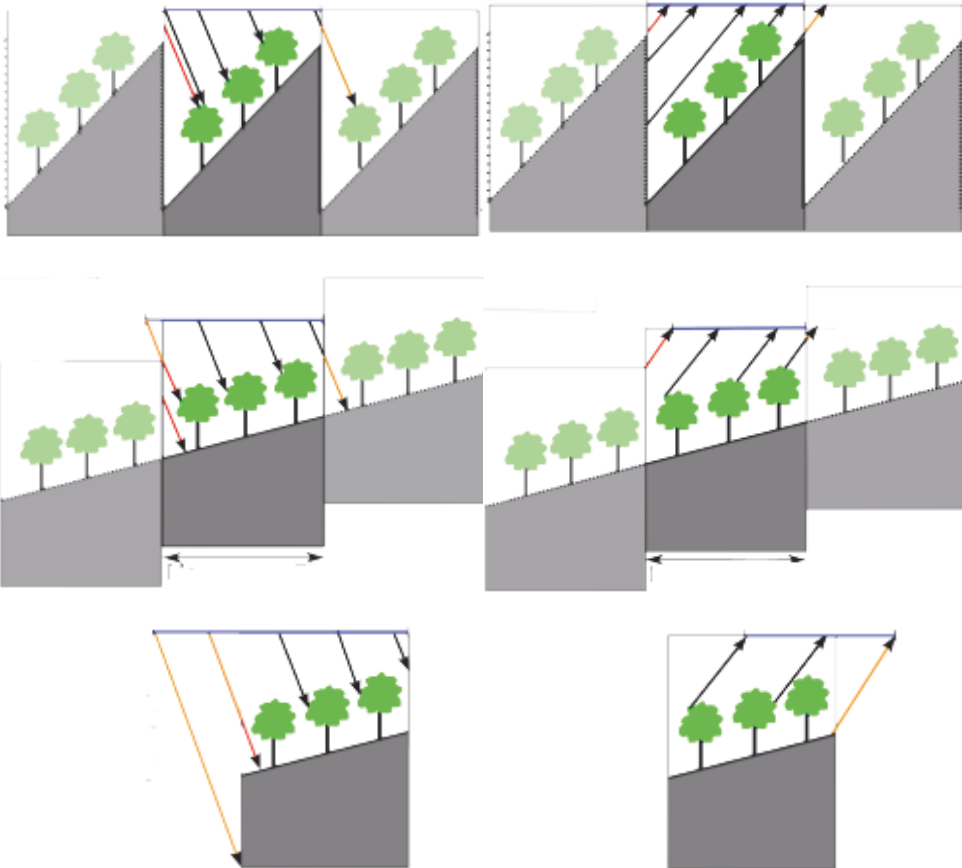


7 Fig. 11. 3D triangle and turbid simulations in the blue (B0), green (B1) and red (B2) spectral
8 bands of the citrus plot. a) 3D triangle scene. d) Derived 3D turbid scene. Associated nadir
9 (b, e) and oblique (g, h) color composite of the DART simulated images. c, f) Associated 2D
10 reflectance polar plots.

11 4.3 Finite landscapes and continuous infinite landscapes topography

12 DART was designed to operate with infinite scenes that are made of a DART simulated
13 pattern that is periodic. When a ray exits the scene, it re-enters the scene by the scene
14 opposite side. This is the so-called "repetitive topography" method. This approach is used in
15 most 3D models. It works very well with landscapes without topography or if the
16 topography is identical on the landscape opposite sides. Thus, it is erroneous in presence of
17 any topography. It is also erroneous if one wants to simulate a finite landscape without
18 interaction with their neighborhood. We solved these 2 problems by introducing 2 new
19 landscape modeling methods, called "Continuous topography" and "Isolated landscape",
20 respectively. This implied to adapt the 3 DART RT modeling modes (*i.e.*, flux tracing, Monte
21 Carlo and lidar). In short, landscapes can be simulated with 3 methods (Figure 12):

- 1 - Repetitive topography: the landscape and the topography are periodic. In that case, a
 2 landscape with a simple slope is actually simulated as a series of periodic slopes, which
 3 implies undesirable illumination (Figure 12.a) and view (Figure 12.b) effects.
 4 - Continuous topography: repetitive landscape with a continuous topography. It allows
 5 one to simulate more realistic landscapes such as infinite slopes. This method is well
 6 adapted to landscapes such as mountain slopes.
 7 - Isolated landscape: no influence of the neighborhood.
 8



14 Fig. 12. The 3 methods of landscape simulation in DART. Top: Repetitive landscape.
 15 Middle: Continuous topography. Bottom: Isolated landscape. Left and right columns
 16 illustrate the illumination and view configurations.

17 Figure 13 illustrates the 3 methods for simulating landscapes. In the image simulated with
 18 the repetitive method, shadow is not continuous on the scene edges, due to the
 19 discontinuity of the slope. It would have been continuous in the absence of topography.
 20 On the other hand, as expected, shadow is continuous with the "Continuous method". As
 21 expected, for the "Isolated landscape", shadow is not continuous (no adjacency effects).

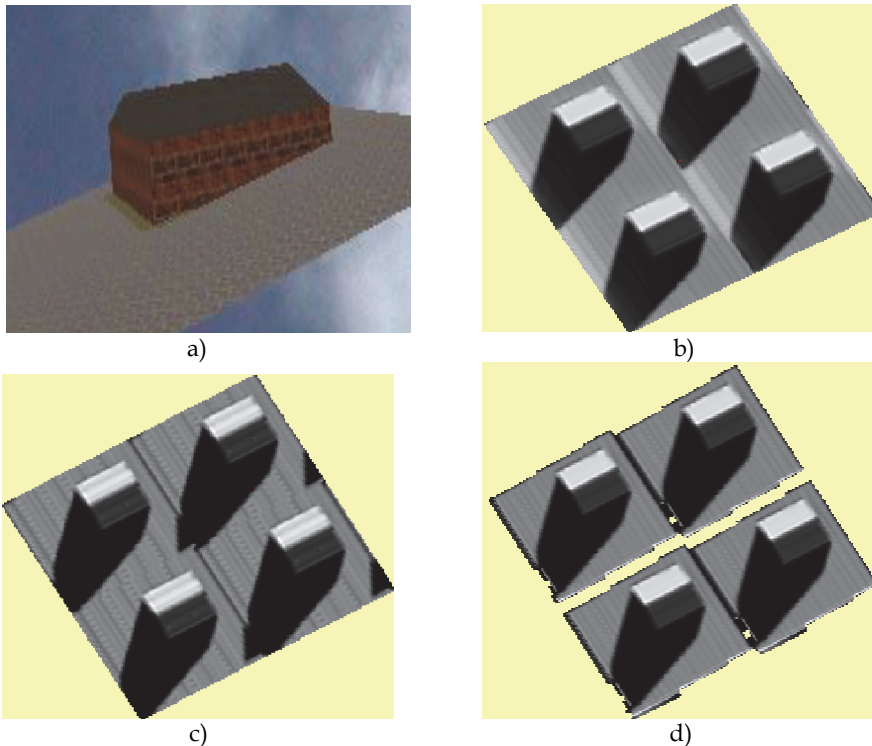
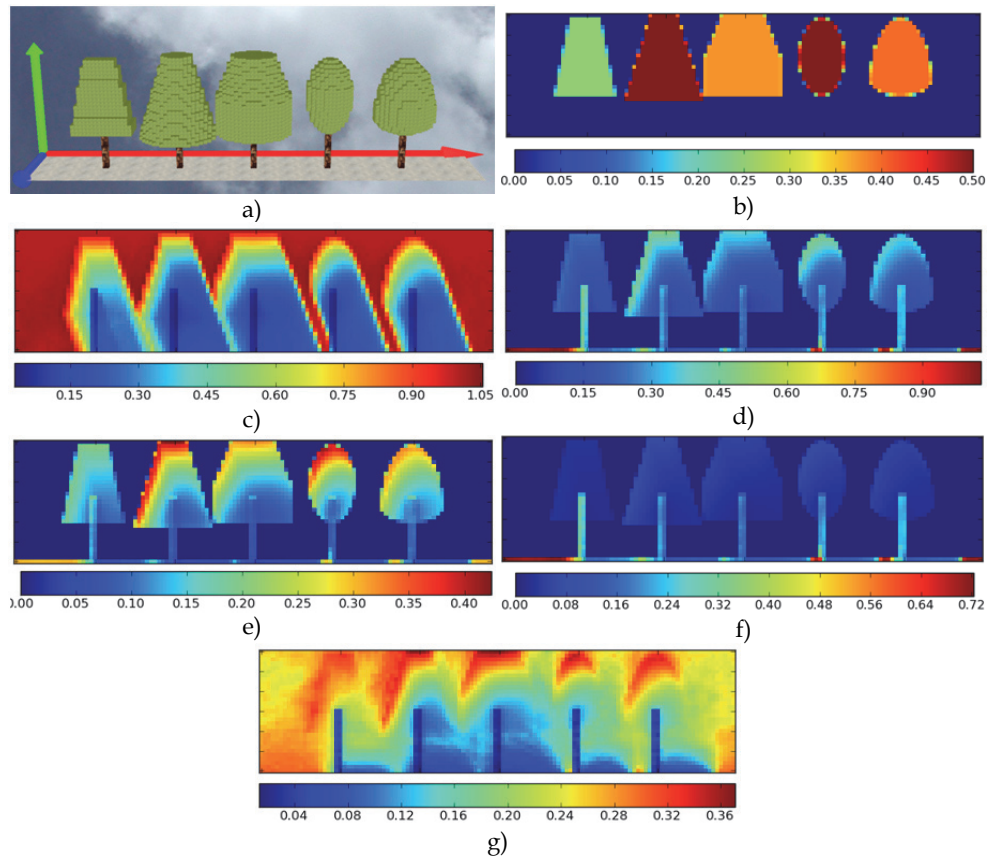


Fig. 13. Simulation of a house on a slope.

a) Scene. b) Repetitive topography. c) Infinite (i.e., continuous) slope. The shadow is not continuous, due to the discontinuity of the slope) Isolated scene (no adjacency effects).

4.4 Radiative budget

Different modules and tools were added to DART for better simulating and managing the 3D radiative budget. DART computes the different terms of the radiative budget: absorbed energy per cell, intercepted energy per cell, scattered energy per cell and downward and upward energy on top cell faces. Here, this is illustrated by a schematic tree landscape (Figure 14). DART simulation was conducted in the near infrared with a SKYL equal to 0.2 and a sun direction ($\theta_s = 160^\circ$, $\phi_s = 90^\circ$). The possibility to obtain 2D and 3D displays is very helpful for understanding the radiation interaction within the tree canopy. For example, here, larger downward radiation occurs in the air cells that are directly illuminated by the sun. This quantity can be larger than 1 because tree crowns scatter radiation through these air cells. Larger interception occurs on the illuminated tree crowns and the ground that is directly illuminated by the sun. Larger scattering occurs where interception is maximal and where local reflectance / albedo is maximal. This explains that scattering by illuminated tree crowns is larger than scattering by the illuminated ground. Indeed, in the near infrared, leaf albedo is larger than ground reflectance. It is interesting to note that the "Broadband" module of DART computes broadband radiation budget with the DART simulated narrow band radiation budgets.



1 Fig. 14. 3D radiative budget of a schematic tree cover. Spatial resolution is $\Delta x=0.5\text{m}$. Ox axis
 2 is in blue color in a). Figures b) to g) show 2D distributions in the plane $x=5\text{m}$ of the ratio
 3 "Radiometric quantity / Irradiance on the top of the landscape. b) LAI_{cell}. Leaf volume
 4 density is LAI_{cell}. Δx . c) Downward energy. d) Intercepted energy. e) Scattered energy.
 5 f) Absorbed energy. g) Upward energy.

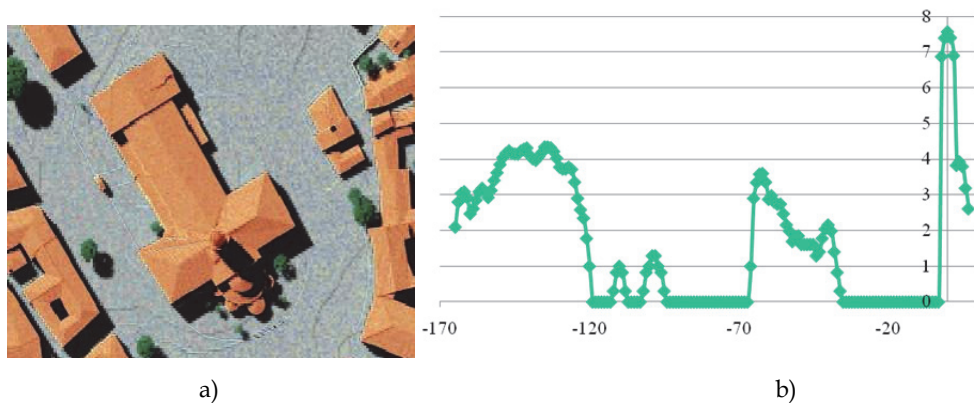
6 4.5 Lidar

7 DART simulates lidar waveforms of urban and natural landscapes. For that, it uses a Monte
 8 Carlo method that is adapted for taking into account the usually strong anisotropy of the
 9 phase function of landscape elements. In short, the occurrence probabilities of scattering
 10 events that have the same order of magnitude are grouped for obtaining groups that have
 11 cumulated probabilities with the same order of magnitude (Gastellu-Etchegorry *et al.*, 2010).
 12 The Monte Carlo mode in the DART model was initially developed for assessing the
 13 accuracy of DART flux tracing method, using the same simulations of landscapes. Indeed,
 14 flux tracing RT modelling requires some simplifying hypotheses for representing multiple
 15 scattering. The associated inaccuracy depends on the trade-off between the expected
 16 accuracy and computational time of simulations. The advantage of the Monte Carlo

1 approach is to simulate multiple scattering processes as a succession of exactly modelled
2 single scattering processes.

3 In order to simulate Lidar waveforms, the DART Lidar module works with a Gaussian
4 spatial distribution for illumination, and a Gaussian (time) laser pulse. It is suited for small
5 and large footprints. It is very flexible because it inherits major features of the DART model:
6 urban and natural scenes, with topography, atmosphere, etc. Examples of waveforms are
7 presented here for urban and natural scenes.

8 Figure 15 illustrates lidar modelling of a urban area that is the St Sernin district (Figure 3). It
9 shows the image that is simulated with the flux tracing mode and the waveform that is
10 simulated with the lidar module. As expected, the horizontal axis of the waveform gives the
11 altitude of scene elements (buildings, vegetation, ground).
12
13

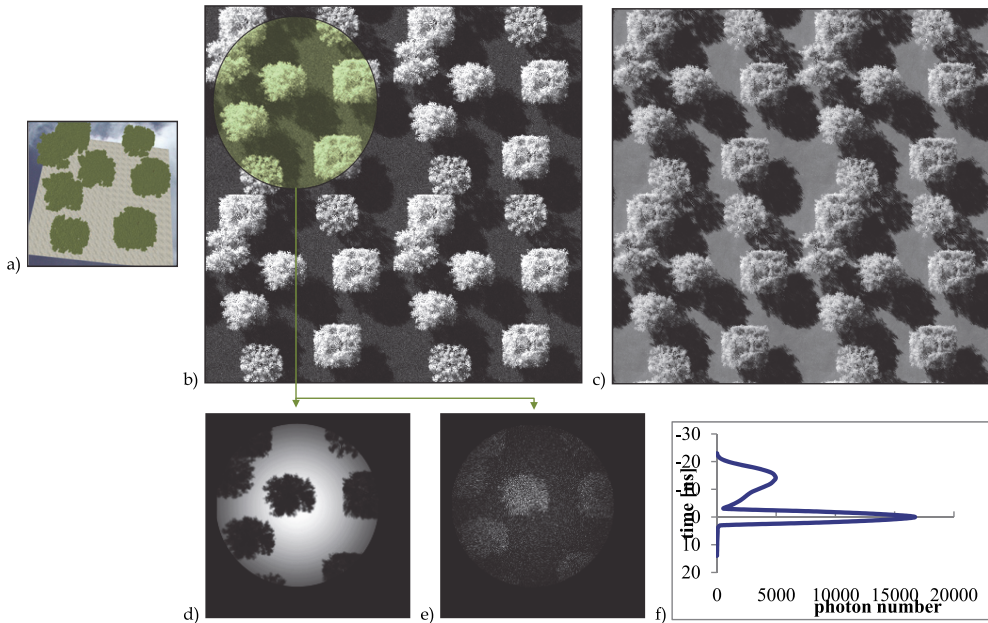


14
15
16

17 Fig. 15. DART lidar simulation of the St Sernin district. a) Image simulated with the flux
18 tracing mode. b) Waveform (Ox: time (ns), Oy: power (logarithmic)). Ground gives the
19 larger peak. Top point (Basilique) gives the 1st signal.

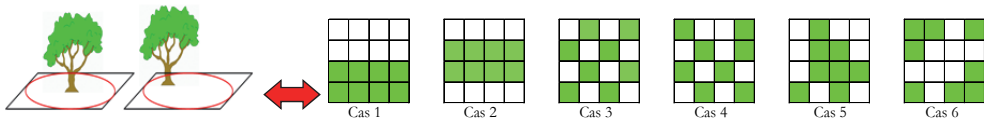
20 Lidar simulation of a plot of citrus trees is shown here (Figure 20.a). Figure 20 b and c show
21 the DART images simulated with the Monte Carlo mode and with the flux tracing mode.
22 The 2 images are very similar. Actually, the degree of similarity depends on the number of
23 photons that are used. As expected, the Monte Carlo mode is usually much more expensive
24 in terms of computation time. An interesting point is that DART simulates the images of the
25 illuminated and view footprints (Figure 20 d and e). This is very useful for interpreting the
26 simulated waveform (Figure 20 f). As expected, the latter one shows a peak that corresponds
27 to the ground and a peak that corresponds to the tree crowns.

28 The citrus waveform (Figure 16.f) being related to the LAI (Leaf Area Index) vertical profile,
29 Ueberschlag (2010) assessed the potential of DART for retrieving the LAI of forests with an
30 inversion procedure. Results were encouraging. As expected, similarly to the lidar response,
31 the LAI retrieval depends a lot on the location of trees within the footprint, except if the
32 lidar signal is uniform. For a Gaussian lidar signal, Figure 17 shows that in the case of a tree
33 cover the LAI of which is 0.5, the retrieved LAI can vary from 0.33 up to 0.70, depending on
34 the tree location within the footprint.



1
2
3
4
5
6
7
8

Fig. 16. Lidar simulation of citrus trees (a). Images simulated with the Monte Carlo mode (b) and the flux tracing mode (c). Images of Lidar ground (d) and view area (e) footprint. Waveform (f). The lidar has a 3ns pulse duration, a 0.5ns acquisition rate, a 4m footprint radius and a 0.368 Gaussian illumination parameter.



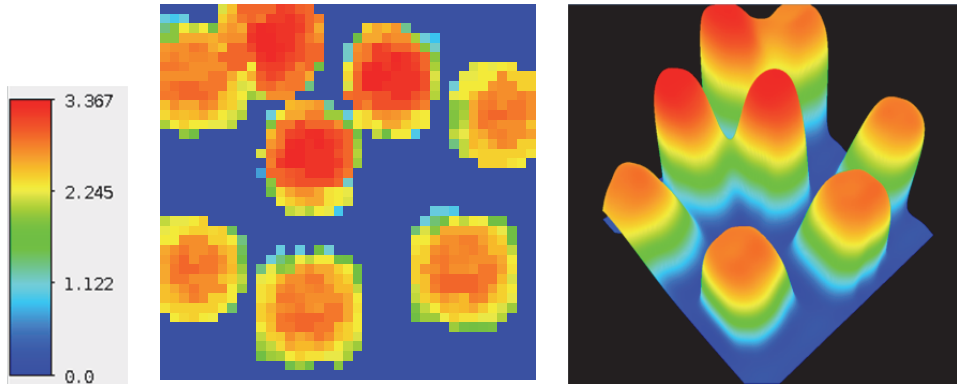
9
10
11

Case	1	2	3	4	5	6
Theoretical LAI	0,5	0,5	0,5	0,5	0,5	0,5
Retrieved LAI - Gaussian signal	0,52	0,70	0,50	0,45	0,64	0,33
Absolute error (%) - Gaussian signal	4,5	40,1	-0,2	-10,4	28,2	-33,8
Retrieved LAI - Uniform signal	0,5	0,5	0,5	0,5	0,5	0,5
Absolute error (%) - Uniform signal	0	0	0	0	0	0

Fig. 17. Influence of vegetation location in the lidar footprint for retrieving forest LAI with DART.

The potential of altitude mapping was assessed. Figure 18.a shows an altitude map where the altitude of each pixel is the local higher altitude. This is called the Lidar first return altitude map. Figure 18.b is an interpolation of Figure 18.a for obtaining a 3D display.

16



1 Fig. 18. Altitude mapping from DART waveforms. a) Height scale. b) Lidar first return
 2 altitude map: resolution 0.25*0.25m. c) Lidar interpolated altitude 3D map

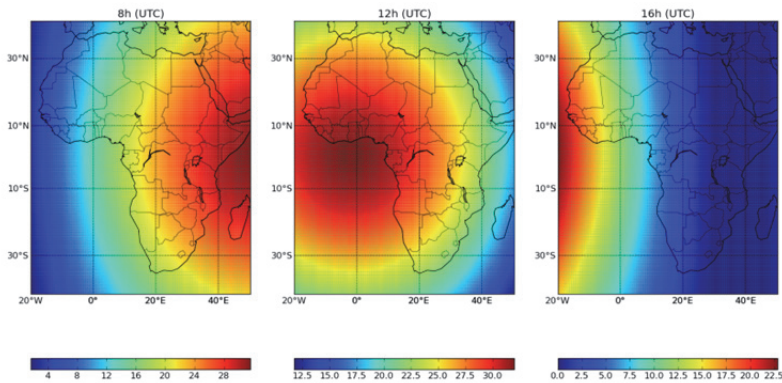
3 **5. Examples of applications**

4 **5.1 Radiance and radiative budget at continental scale**

5 A method was developed to create automatically for every spectral band, any date and any
 6 land area, maps of radiometric products (*i.e.*, radiance, reflectance, brightness temperature)
 7 at a continental scale. For that, it realizes a spatial interpolation on a set of georeferenced
 8 DART products that are created by running the DART "sequencer" module with time,
 9 wavelength and land surface location used as variable parameters.

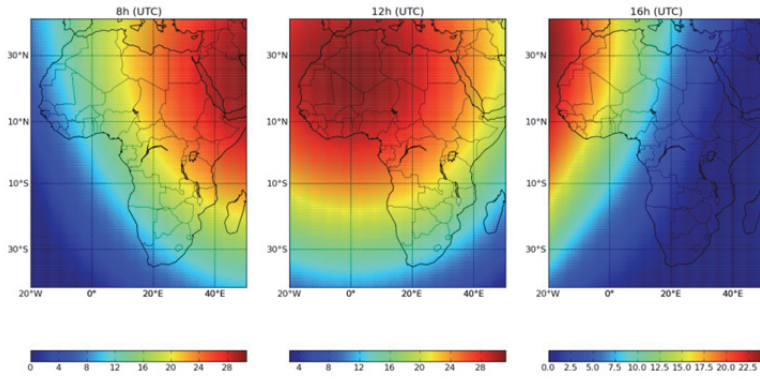
10 Results shown here are for the African continent, with a geostationary satellite (35800km
 11 altitude, 0° N, 17° E) for 2 spectral bands (550nm: Figure 19 and Figure 20; 900nm: Figure 21
 12 and Figure 22) at 4 dates: March 21 2011 (spring equinox), June 21 2011 (summer solstice),
 13 September 21 2011 (autumn equinox) and December 21 2011 (winter solstice), at 3 daytimes
 14 (8hUTC, 12hUTC, 16hUTC). The atmosphere is defined by a US Standard gas model and
 15 rural aerosols with a 23km visibility. Simulations were carried out with the ground
 16 horizontal Lambertian "Brown to dark brown gravelly loam" from the USDA Soil
 17 Conservation Service): $\rho_{\text{ground},550} = 0.061$ and $\rho_{\text{ground},900} = 0.351$.

18

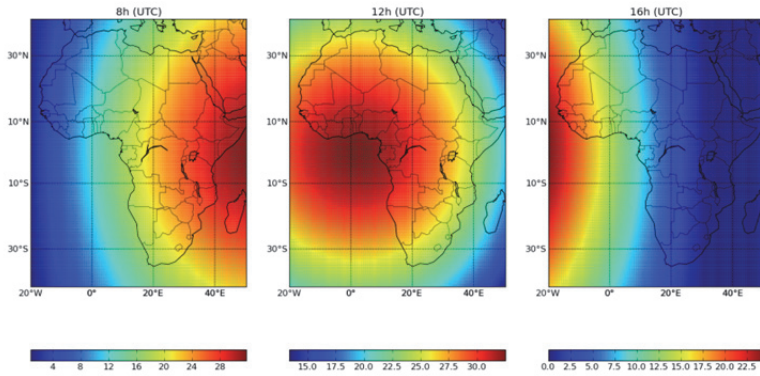


a)

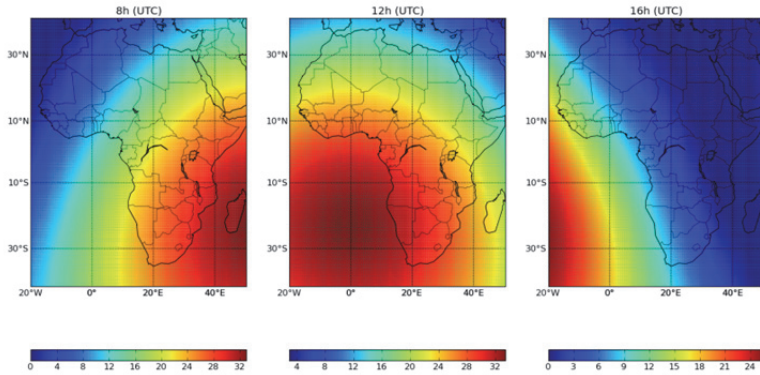
19
 20



b)



c)



d)

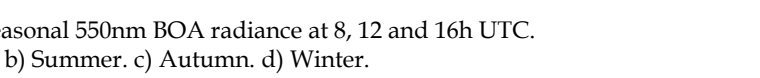


Fig. 19. Seasonal 550nm BOA radiance at 8, 12 and 16h UTC.
 a) Spring. b) Summer. c) Autumn. d) Winter.

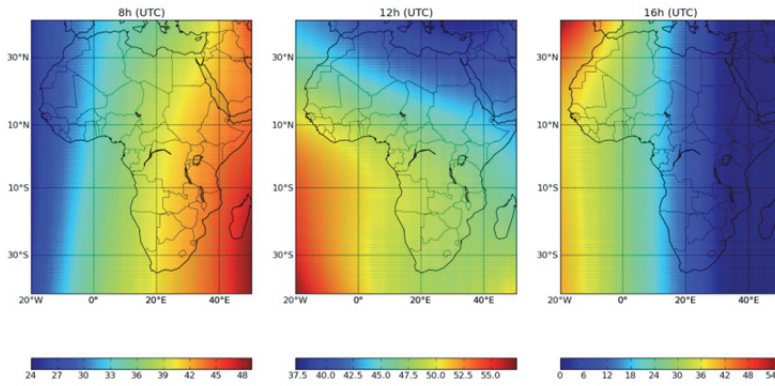
1
2
3

4
5
6

7
8
9

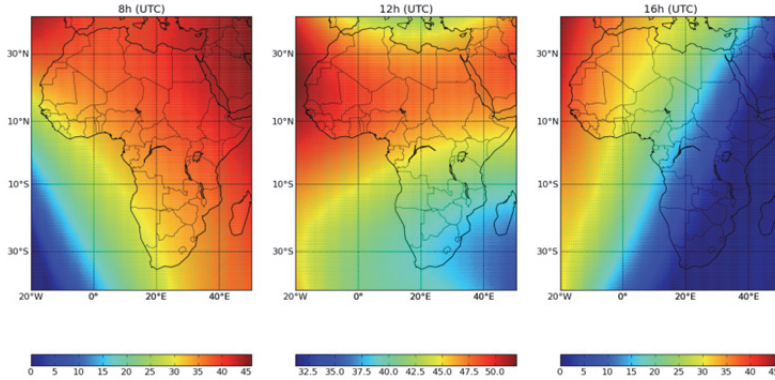
10
11

1



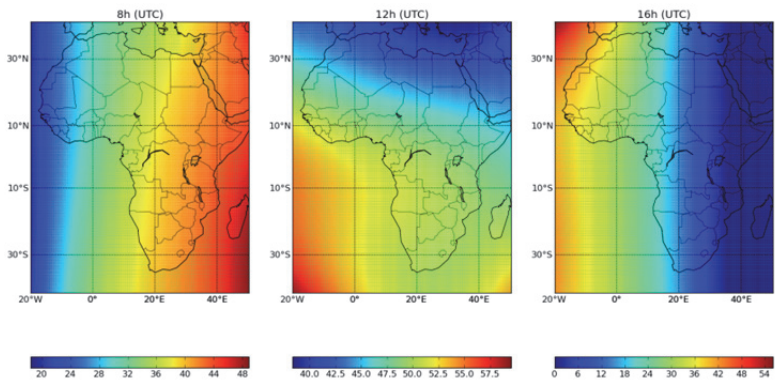
2
3
4

a)



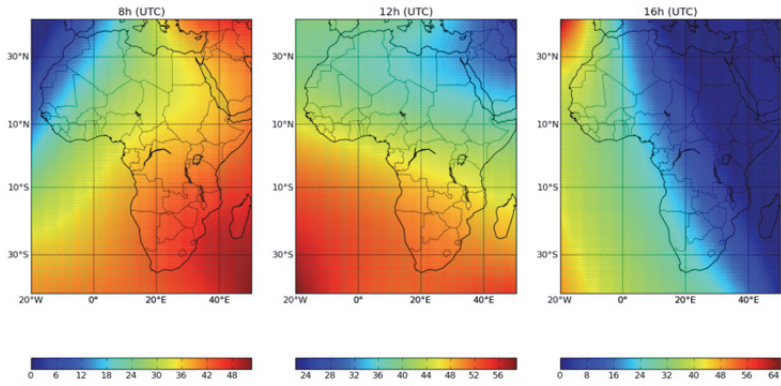
5
6
7

b)



8
9

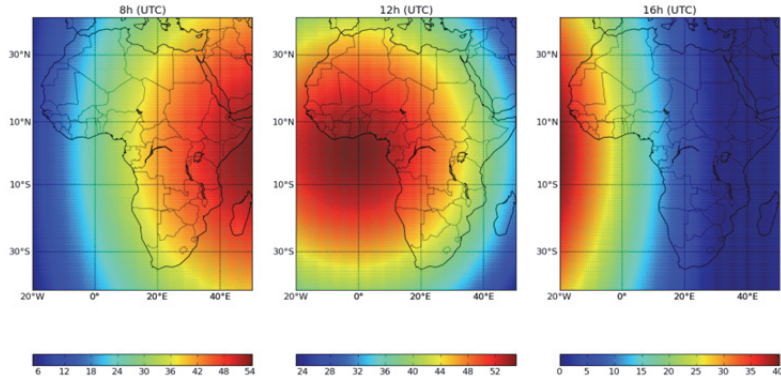
c)



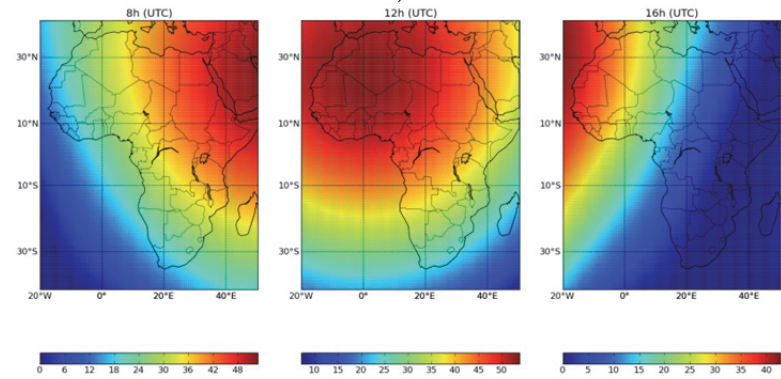
d)

Fig. 20. Seasonal TOA 550nm radiance at 8, 12 and 16h UTC.

a) Spring. b) Summer. c) Autumn. d) Winter.



a)



b)

1
2

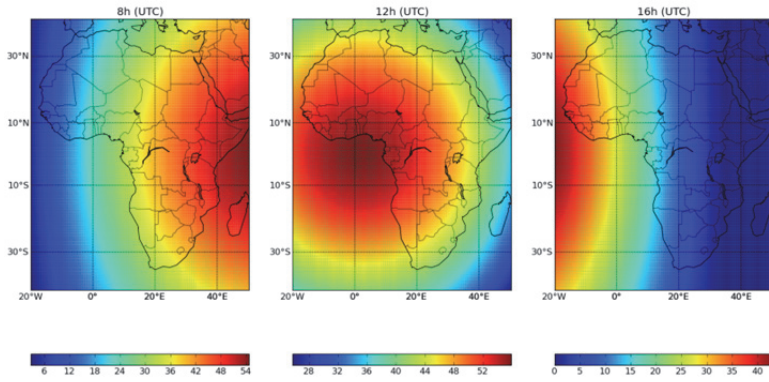
3
4

5

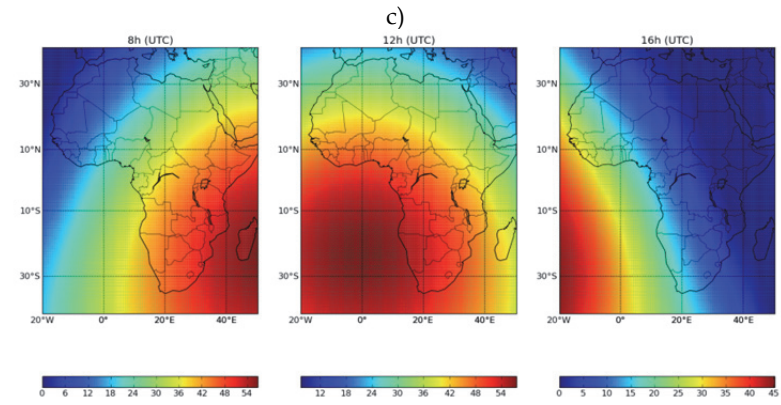
6
7

8
9

1
2



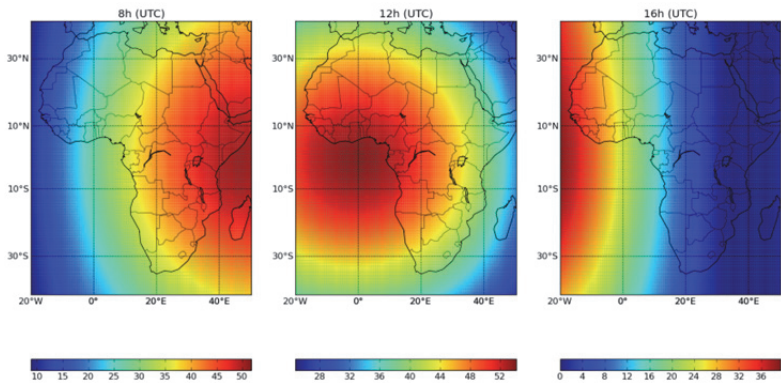
3
4



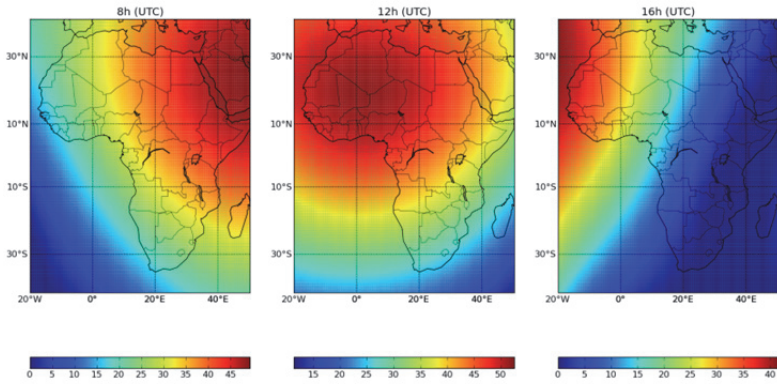
5
6
7

Fig. 21. Seasonal BOA 900nm radiance at 8, 12 and 16h UTC.
a) Spring. b) Summer. c) Autumn. d) Winter.

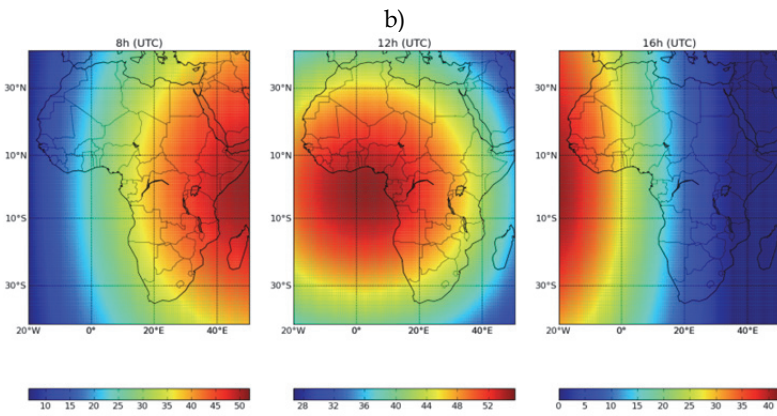
8
9



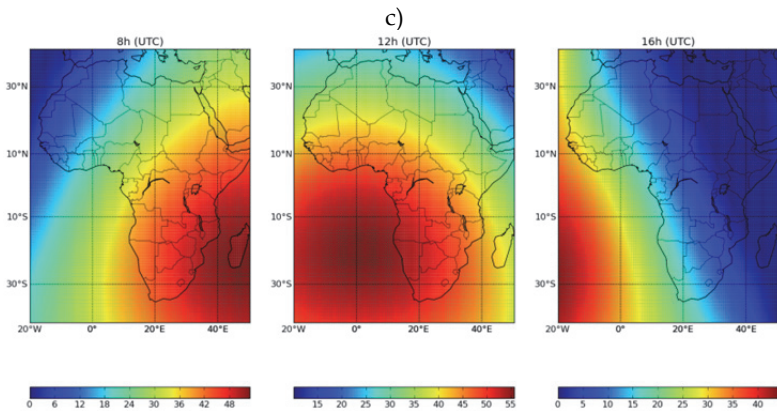
a)



1
2



3
4



5
6

d)

7 Fig. 22. Seasonal TOA 900nm radiance at 8, 12 and 16h. a) Spring. b) Summer. c) Autumn. d)
8 Winter.

1 In a 1st step, the tool "Sequencer" created a grid of 20x20 DART simulations at 5 wavelengths
2 (0.4 μ m, 0.55 μ m, 0.67 μ m, 0.9 μ m, 1.65 μ m, 11 μ m), with an automatic computation of the sun
3 and view sensor angles in the local reference system, as a function of the date, time and
4 coordinates. The grid covers almost all of the African continent: "40° S - 44° N" in latitude
5 (step of 4.2°) and "20° W - 54° E" in longitude (step of 3.7°). In a 2nd step, the grid of DART
6 products is interpolated (Python script and Numpy module). Results are displayed with a
7 Python script and the module Basemap.

8 Logically, TOA radiances differ a lot from BOA radiances, because of the atmosphere.
9 Moreover, one can note:

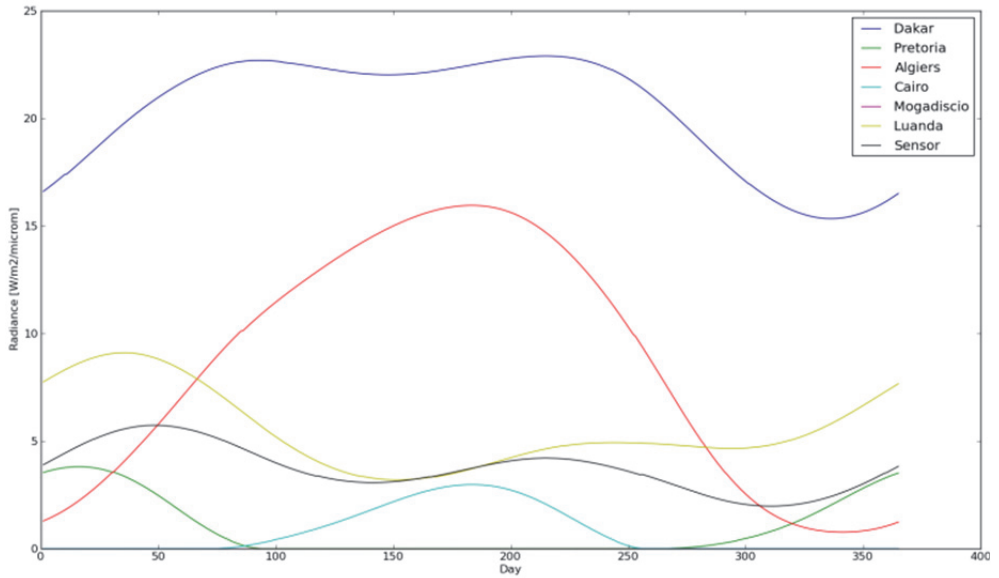
- 10 - BOA radiances are maximal in the East in the morning and West in the evening. During
11 summer, they are larger in the Northern Hemisphere and lower in the Southern
12 hemisphere. The situation is reversed in winter.
- 13 - TOA radiances tend to be maximal in the East in the morning and in the West in the
14 evening. This effect is less clear than for BOA radiances. During summer, TOA
15 radiances are larger in the Northern Hemisphere and lower in the southern hemisphere.
16 The situation is reversed in winter.

17 The impact of atmosphere on TOA radiances depends on its optical thickness and phase
18 function and on the sun and view directions. The analysis of DART images allows
19 one to verify that this impact is not symmetric from the point of view of the satellite
20 sensor.

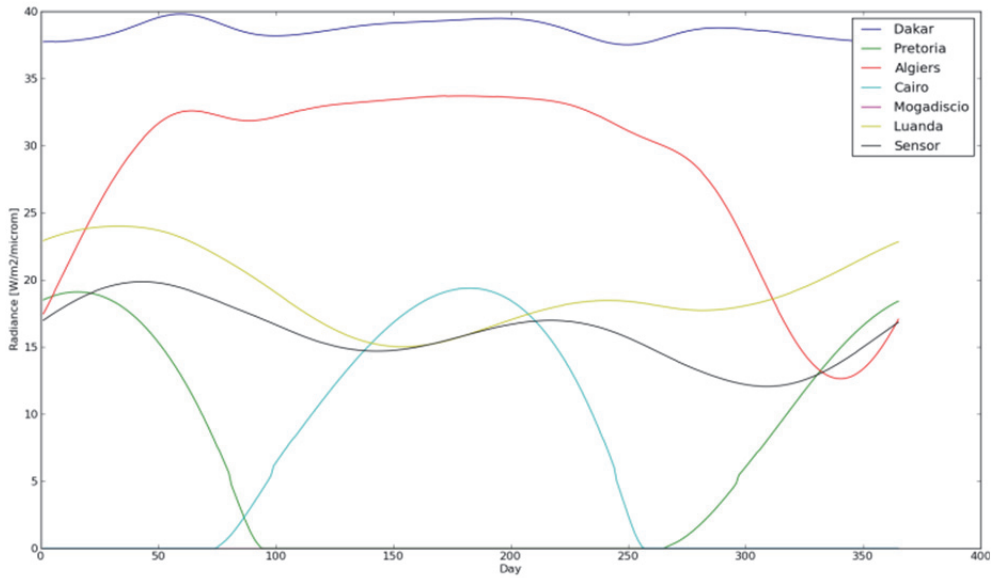
21 The Figure 11 and Figure 12 show the maps of luminance to 900nm of the African
22 continent to 4 dates (spring, summer, autumn, winter) and 3:00 (UTC 8h, 12h UTC 16h
23 UTC) defined above. As Figure 9 and Figure 10, this is 100 * 100 maps obtained by
24 interpolation of DART simulations performed for 400 geographical sites, with a
25 Lambertian soil ($\rho = 900$ 0351: "Brown to dark brown gravelly loam" of USDA Soil
26 Conservation service) and an atmosphere "US Standard" with aerosols 23km visibility.
27 Logically, the TOA radiances and reflectances are much less affected by the atmosphere in
28 the near infrared than in the field of green. The spatial variability of radiances is mainly
29 due to the spatial variability of the illumination of the land surface. The geometric
30 configuration "Sun - Earth" plays a much more important role than the geometric
31 configuration "Sensor - Sun-Atmosphere". This is particularly the case of the phase
32 function of gases and aerosols. This explains the much larger symmetry of the near-
33 infrared maps of luminance.

34 Figure 23 shows the annual evolution of BOA (a) and TOA (b) radiances of 6 cities: Algiers
35 (36.42° N, 3.13° E, UTC +1), Cairo (30.2° N, 31.13° E; UTC +2), Dakar (14.4° N, 17.25° W,
36 UTC), Pretoria (25.45° S, 28.11° E, UTC +2), Mogadishu (2.02° N 45.21° E, UTC +3),
37 Luanda (8.50° S, 13.14° E, UTC +1). The evolution of the radiance $L_{ref}(t)$ at the nadir of the
38 satellite sensor is used as a reference. Any radiance $L(t)$ larger than $L_{ref}(t)$ indicates that the
39 sensor receives light above this reference.

40 Figure 24 shows the 11 μ m TOA radiance, and its associated Brightness temperature, of the
41 African continent. It was obtained with a ground surface characterized by an emissivity
42 equal to 1 and a 300K thermodynamic temperature, a US standard atmosphere and an
43 atmosphere water vapor thickness equal to 1.4cm. The simplicity of this configuration
44 explains the spatial symmetry of brightness and temperature. Indeed, one should take into
45 account the actual local emissivity and thermodynamic temperature.



a)



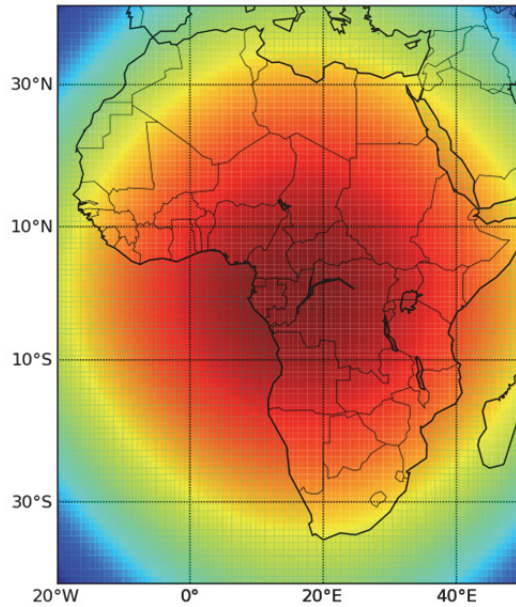
b)

1
2
3
4

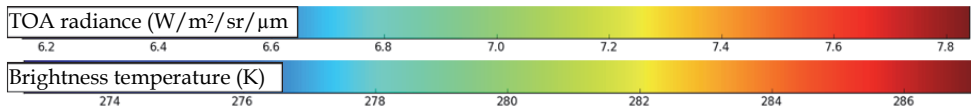
5
6
7
8

9 Fig. 23. 550nm BOA (a) and TOA (b) radiance of 7 cities at 16h UTC over1 year.

1
2
3



4
5
6



7
8
9

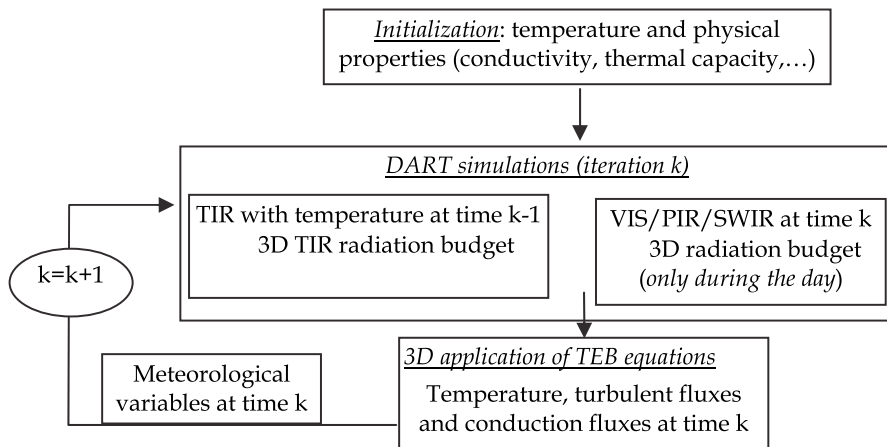
10 Fig. 24. $11\mu\text{m}$ TOA radiance (a) and associated brightness temperature (b).

11 5.2 DARTEB energy budget simulation

12 Energy budget modeling is essential for many application domains such as the functioning
 13 of land surfaces. It is also essential for obtaining realistic simulations of satellite
 14 measurements in the thermal infrared. Indeed, it allows one to obtain the 3D distribution of
 15 thermodynamic temperature. This explains present efforts for developing a model, called
 16 DARTEB (DART Energy Budget), that simulates the 3D radiative budget of urban and
 17 vegetation surfaces, possibly with topography and atmosphere. DARTEB uses the 3-D
 18 DART radiative budget and it models all physical phenomena, other than radiation, that
 19 contribute to the energy budget: heat conduction, turbulent momentum and heat fluxes,
 20 water reservoir evolution, vegetation photosynthesis, evapotranspiration. The example
 21 shown here is for a urban canopy. In that case, non-radiative mechanisms that contribute to
 22 the energy budget are simulated with the equations of the TEB urban surface scheme
 23 (Masson, 2000). This scheme works with a canyon geometry. For example, turbulent fluxes
 24 and conduction are computed with classical boundary-layer laws using equations of TEB.

1 Conversely to the TEB scheme, DARTEB uses a 3-D cell discretization, in addition to the
 2 layer discretization of roofs, walls and roads: modeling is conducted on a DART cell per cell
 3 basis. As a result, fluxes are computed for each point of the 3-D scene. The transfer
 4 coefficients for turbulent heat and moisture fluxes are identical; they differ from the transfer
 5 coefficients for momentum fluxes. For DARTEB, the urban canopy is simulated as the
 6 juxtaposition of urban street canyons. Here, we worked with a single urban canyon, for
 7 remaining in the validity domain of TEB equations (Masson, 2000). Each surface type (wall,
 8 soil, roof) is discretized into several layers for simulating the conduction fluxes to or from
 9 the ground and building interiors. The number of layers for road, wall and roof can differ. A
 10 minimal number of three layers is advised because temperature gradients can be large and
 11 because of the multi-layer structure of the walls and roofs.

12 DARTEB uses a prognostic approach for assessing the 3D radiative budget distribution, and
 13 consequently the 3D temperature distribution. Temperature values at time " $k - 1$ " are used
 14 for computing the 3D TIR and energy budgets at time " k ", which allows one to compute the
 15 3D temperature distribution at time " k ", using the 3D visible and NIR radiation budget at
 16 time " k " (Figure 25). DART simulations in the short wave domain are conducted during the
 17 day period only.
 18
 19
 20

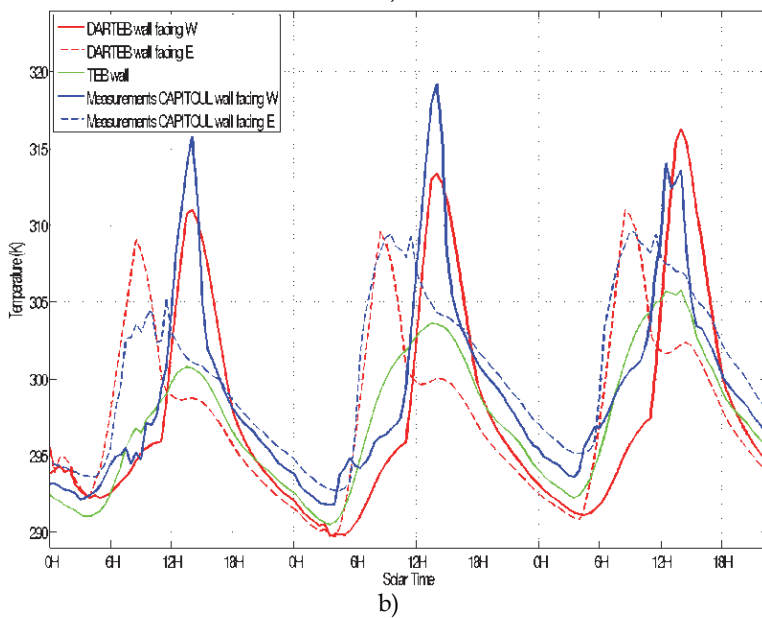
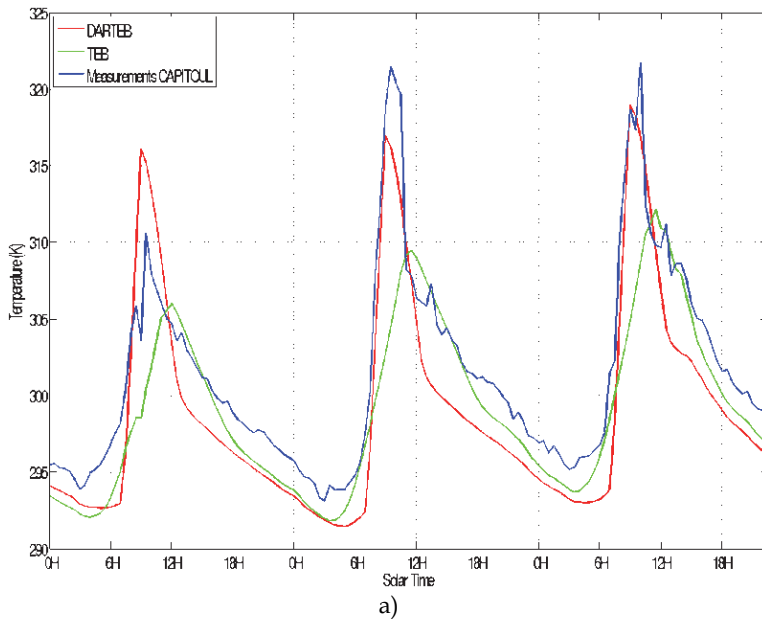


21
 22
 23

24 Fig. 25. Diagram of DARTEB model.

25 The validity of DARTEB was tested against TEB simulations and against in situ temperature
 26 measurements during the Capitoul campaign (Albinet, 2008). DARTEB proved to be
 27 coherent with TEB and with measurements. Here, this is illustrated by the comparison of
 28 simulated and measured temperatures during 3 days, from July 14 to July 17, 2004, for the
 29 Alsace Lorraine street (South-North orientation) and La Pomme street (South East - North
 30 West orientation) in Toulouse.

31 The simulated and measured road temperature curves are very similar (Figure 26.a). As
 32 expected, road temperature values increase during the day. There are 3 major differences



5 Fig. 26. Comparison of temperature measurements (blue) with DARTEB (red) and TEB
6 (green) simulations. July 14-16 2004. a) Road of La Pomme street (Toulouse) with a south
7 East - North West orientation. b) Walls of Alsace Lorraine street (Toulouse) with a South-
8 North orientation. The 2 walls are facing West and East directions, which implies different
9 thermal behaviors.

1 between DARTEB and TEB simulations. (1) Maximal DARTEB temperatures are larger than
2 maximal TEB temperatures. (2) Maximal DARTEB temperatures occur before midday
3 conversely to maximal TEB temperatures that occur at midday. (3) DARTEB curves are
4 smoother than TEB curves. These differences are mostly explained by the fact that DARTEB
5 takes into account the 3-D nature of the canyon geometry, conversely to TEB. Indeed, the
6 TEB model works with a mean canyon that corresponds to an azimuthally averaged street
7 direction. Thus, TEB temperatures are mean values, which explains that their time
8 variations are smoothed, with maximal values at midday. Actually, due to the South East -
9 North West orientation of La Pomme street, the maximum road illumination occurs before
10 midday and the maximal road illumination is larger than the mean road illumination for all
11 possible canyon orientations. This is well simulated by DARTEB. Each morning, the
12 measured and DARTEB temperature values display nearly the same sharp increase.
13 However, each afternoon, DARTEB temperature values decrease faster than TEB and the
14 observed temperature values. Several factors can explain the differences between
15 the DARTEB and observed temperature values. For example, an inaccurate road heat
16 capacity implies an inaccurate conduction flux, and an inaccurate road roughness length
17 tends to imply an inaccurate heat flux, which tends to lead to inaccurate road temperature
18 values. Another possible explanation can come from an inaccurate simulation of the
19 proportions of the 2 components of the canyon illumination: sun and sky illumination.
20 Here, these components are driven by the atmosphere optical depth and sun zenith angle.
21 However, in the absence of measurements, the atmosphere optical depth is assumed to be
22 constant.

23 The wall (Figure 26.b) DARTEB and measured temperature values tend to be very close,
24 both for the wall facing West, and for the wall facing East. They differ from TEB
25 temperature values because TEB gives a mean value for the 2 walls of the canyon.
26 Account of wall orientation is important because walls with different sun illumination
27 have different temperature values, with larger values during daytime for walls with best
28 sun orientation. As expected, DARTEB maximal temperature values occur in the morning
29 for the wall facing East, and in the afternoon for the wall facing West. This is not the case
30 with TEB maximal temperature values; they occur at midday due to the fact that TEB
31 works with azimuthally averaged canyons. This explains also that TEB temperature
32 values are too small. These examples stress the impact of 3-D architecture on temperature
33 distributions.

34 **6. Concluding remarks**

35 Some major and recent improvements of DART radiative transfer model are presented in
36 this paper. After years of development DART has reached the stage of a reference model in
37 the field of remote sensing in the optical domain. It was patented (PCT/FR 02/01181) in
38 2003. It is used in more than 80 Space Centers, Universities and Research Centers: NASA
39 GSFC (USA), the King's College (UK), Research center of Meteo France, IRD (France),
40 Virginia University (USA), Instituto de Agricultura Sostenible (Spain), etc. Paul Sabatier
41 University (France) provides free licenses for scientific works (www.cesbio.ups-tlse.fr), for
42 windows and Linux systems. Its domains of application are centered on remote sensing
43 applications for land surfaces (forestry, agriculture, urbanism,...), on the preparation of
44 future satellite sensors and on the improvement of the use of already available satellite data.
45 It is also more and more used for radiation budget in urban and natural environments, with

1 the objective to couple it with functioning models. Moreover, DART is also more and more
 2 used in the field of education for teaching the physical bases of remote sensing and radiative
 3 budget. Generally speaking, the possibility to create very easily urban and natural
 4 landscapes is very interesting for scientists who want assess remote sensing measurements
 5 in any experimental and instrument conditions.
 6 Today, work continues for improving DART, for both the physics, functionalities and
 7 computer science aspects. Present ongoing improvements concern the storing and
 8 manipulation of LUTs as actual databases, the inversion of satellite images, the Lidar and
 9 the design of a new GUI. Planned improvements concern the modeling of the Earth-
 10 Atmosphere system in presence of clouds. DART will not simulate RT within clouds. These
 11 will be considered as interfaces with specific optical properties and geometric dimensions.
 12 Other major planned improvements will be the simulation of RT adapted to water bodies
 13 and to fire.

14 7. Acknowledgement

15 This work was supported by the Centre National d'Etudes Spatiales (CNES) in the frame of
 16 the project "High spatial resolution of the land surfaces with a geostationary satellite". The
 17 authors are also thankful to team of scientists the Space Center for Biosphere Studies
 18 (CESBIO) who contribute to the development of DART.

19 8. Annex: Computation of view incidence angle

20 For an Earth target T and a satellite sensor S, DART computes the local incidence angle α ,
 21 the sensor off-nadir direction β and the sun azimuth angle in the Earth surface reference
 22 system as a function of the locations (latitude, longitude, altitude) of T and S, with the
 23 assumption that the Earth is an ellipsoid.

24 Let us note O the Earth center and Oz the "South - North" axis perpendicular to the
 25 equatorial plane. The axis Ox is perpendicular to Oz and is in the plane $\{\vec{OT}, \vec{Oz}\}$. The plane
 26 that contains the target T and the vertical Oz is an ellipse defined by $\frac{x^2}{a^2} + \frac{z^2}{b^2} = 1$, with
 27 $a=6378.136\text{km}$ and $b=6356.751\text{km}$. The earth eccentricity is: $e = \frac{\sqrt{a^2-b^2}}{a}$. At local latitude Lat,
 28 the local Earth radius is: $R(Lat) = \frac{b}{\sqrt{1-e^2 \cdot \cos^2(Lat)}}$

29 Any point M on the ellipsoid is characterized by $(\text{Lat}_m, \text{Long}_m)$ or by the angles (γ_m, ϕ_m) in
 30 the Earth spherical coordinate system (Figure 26):

31 $\text{Lat} \in [90^\circ\text{S } 90^\circ\text{N}] \Leftrightarrow \gamma \in [0 \ 180^\circ]$ ($\gamma = 0 \Leftrightarrow \text{Lat} = 90^\circ\text{N}$)

32 $\text{Long} \in [0 \ 360^\circ] \Leftrightarrow \phi \in [0 \ 360^\circ]$

33 Let R_{target} and R_{sat} be the Earth radius at points t and s that are the vertical projection on the
 34 Earth ellipsoid of target T and satellite S respectively. Points t and s are defined by:

35 - t: $\text{Lat}_t, \text{Long}_t$. Target T altitude is H_{target} above the Earth surface

36 - s: $\text{Lat}_{\text{sat}}, \text{Long}_{\text{sat}}$. Satellite altitude is H_{sat} above the Earth surface

37 Zenith angles of vectors \vec{OS} and \vec{OT} , with s and t the vertical projections of points S and T,
 38 are:

39 $\gamma_{\text{sat}} = \frac{\pi}{2} - \text{Lat}_{\text{sat}}$ and $\gamma_t = \frac{\pi}{2} - \text{Lat}_t$ respectively (in radians)

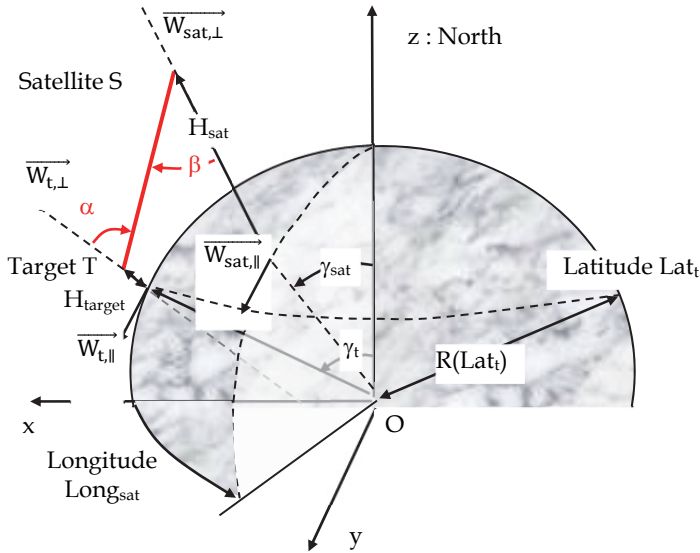


Fig. 27. Geometric configuration "Satellite - Earth scene", for an ellipsoidal Earth.

In the pre-defined Earth system, point t is defined by $\vec{OT} \{R_t(\gamma_t) \cdot \sin(\gamma_t), 0, R_t(\gamma_t) \cdot \cos(\gamma_t)\}$. The unit vector $\vec{W}_{t,||}$ of the tangent to the ellipse along the axis Ox at point t is defined by:

$$- \quad z_t \neq 0: \vec{W}_{t,||} \left\{ 1, 0, -\frac{b^2 x_t}{a^2 z_t} \right\} \cdot \frac{1}{\sqrt{1 + \left[\frac{b^2 x_t}{a^2 z_t} \right]^2}} \quad \text{We note that } \vec{W}_{t,||} \{0, 0, 1\} \text{ if } x_t = 0 \text{ (i.e., } z_t = b)$$

$$- \quad z_t = 0 \text{ (i.e., } x_t = a): \vec{W}_{t,||} \{1, 0, 0\}$$

$$\text{The unit vector } \vec{W}_{t,\perp} \text{ perpendicular to the ellipse at point } t \text{ is: } \vec{W}_{t,\perp} \left\{ 1, 0, -\frac{a^2 z_t}{b^2 x_t} \right\} \cdot \frac{1}{\sqrt{1 + \left[\frac{a^2 z_t}{b^2 x_t} \right]^2}}$$

Let γ_t^* be the zenith angle of $\vec{W}_{t,\perp}$ in the Earth system. It allows one to compute \vec{OT} :

$$\vec{OT} = \vec{Ot} + \{h_t \cdot \sin(\gamma_t^*), 0, h_t \cdot \cos(\gamma_t^*)\} \quad \text{with } \cos(\gamma_t^*) = \vec{W}_{t,\perp} \cdot \vec{W}_z \quad \text{and } \gamma_t^* \in [0, \pi]$$

Similarly, for point s , we have: $\vec{Os} \{R_{\text{sat}} \cdot \sin(\gamma_{\text{sat}}) \cdot \cos(\text{Long}_{\text{sat}} - \text{Long}_t), R_{\text{sat}} \cdot \sin(\gamma_{\text{sat}}) \cdot \sin(\text{Long}_{\text{sat}} - \text{Long}_t), R_{\text{sat}} \cdot \cos(\gamma_{\text{sat}})\}$

1 Let $\overrightarrow{W_{sat,\perp}}$ be the perpendicular to the ellipse at point s in the Earth system. In the local
2 reference:

$$3 \quad (Z - Z_{sat}) = \frac{a^2 \cdot z_{sat}}{b^2 \cdot X_{sat}} (X - X_{sat}) \Rightarrow \overrightarrow{W_{sat,\perp}} \left\{ 1, 0, -\frac{a^2 \cdot z_{sat}}{b^2 \cdot X_{sat}} \right\} \cdot \frac{1}{\sqrt{1 + \left[\frac{a^2 \cdot z_{sat}}{b^2 \cdot X_{sat}} \right]^2}} \text{ if } X_{sat} \neq 0.$$

4 with $X_{sat}^2 = x_{sat}^2 + y_{sat}^2 = R^2(\text{Lat}_{sat}) \cdot \sin^2(\gamma_{sat})$, $x_{sat} = R(\text{Lat}_{sat}) \cdot \sin(\gamma_{sat}) \cdot \cos(\text{Long}_{sat} - \text{Long}_t)$ and y_{sat}
5 $= R(\text{Lat}_{sat}) \cdot \sin(\gamma_{sat}) \cdot \sin(\text{Long}_{sat} - \text{Long}_t)$

$$6 \quad \text{Thus, we have: } \overrightarrow{W_{sat,\perp}} \left\{ \cos(\text{Long}_{sat} - \text{Long}_t), \sin(\text{Long}_{sat} - \text{Long}_t), \frac{a^2 \cdot z_{sat}}{b^2 \cdot X_{sat}} \right\} \cdot \frac{1}{\sqrt{1 + \left[\frac{a^2 \cdot z_{sat}}{b^2 \cdot X_{sat}} \right]^2}}$$

7 It implies: $-\overrightarrow{OS} = \overrightarrow{OS} + \{H_{sat} \cdot \sin(\gamma_{sat}^*) \cdot \cos(\text{Long}_{sat} - \text{Long}_t), H_{sat} \cdot \sin(\gamma_{sat}^*) \cdot \sin(\text{Long}_{sat} -$
8 $\text{Long}_t), H_{sat} \cdot \cos(\gamma_{sat}^*)\}$

9 This allows one to compute the incidence angle α , the sensor off-nadir angle β and the
10 satellite azimuth φ_{sat} in the local system:

$$11 \quad \cos(\alpha) = \frac{\overrightarrow{TS} \cdot \overrightarrow{W_{t,\perp}}}{\|\overrightarrow{TS}\| \cdot \|\overrightarrow{W_{t,\perp}}\|} \Rightarrow \alpha = \text{acos}\left(\frac{\overrightarrow{TS} \cdot \overrightarrow{W_{t,\perp}}}{\|\overrightarrow{TS}\| \cdot \|\overrightarrow{W_{t,\perp}}\|}\right) \text{ with } \alpha \in [0 \ 90^\circ] \text{ and } \overrightarrow{TS} = \overrightarrow{OS} - \overrightarrow{OT}$$

$$12 \quad \cos(\beta) = \frac{\overrightarrow{TS} \cdot \overrightarrow{W_{sat,\perp}}}{\|\overrightarrow{TS}\| \cdot \|\overrightarrow{W_{sat,\perp}}\|} \Rightarrow \beta = \text{acos}\left(\frac{\overrightarrow{TS} \cdot \overrightarrow{W_{sat,\perp}}}{\|\overrightarrow{TS}\| \cdot \|\overrightarrow{W_{sat,\perp}}\|}\right) \text{ with } \beta \in [0 \ 90^\circ]$$

$$13 \quad \overrightarrow{W_{t,\perp}} \cdot \frac{\overrightarrow{TS}}{\|\overrightarrow{TS}\|} = -\sin(\alpha) \cdot \cos(\varphi_{sat}) \Rightarrow \varphi_{sat} = \text{acos}\left(-\overrightarrow{W_{t,\perp}} \cdot \frac{\overrightarrow{TS}}{\|\overrightarrow{TS}\|} \cdot \frac{1}{\sin(\alpha)}\right) \text{ with } \varphi_{sat} = 2\pi - \varphi_{sat} \text{ if}$$

14 $\text{Long}_t < \text{Long}_{sat}$

15 8. References

- 16 Albinet C. (2008). Modélisation 3D des flux et du bilan d'énergie des zones urbaines
17 Modélisation des échanges d'énergie des milieux urbains. M2 report. Paul Sabatier
18 University, Toulouse, France. 57p.
- 19 Barbier, N.; Couteron, P.; Proisy, C.; Yadvinder, M. & Gastellu-Etchegorry, J-P. (2010). The
20 variation of apparent crown size and canopy heterogeneity across lowland
21 Amazonian forests. *Global Ecology and Biogeography*, DOI: 10.1111/j.1466-
22 8238.2009.00493.
- 23 Barbier, N.; Couteron, P.; Gastellu-Etchegorry J.P. & Proisy, C. (2011), Linking canopy
24 images to forest structural parameters: potential of a modeling framework, *Annals*
25 *of Forest Science*, DOI 10.1007/s13595-011-0116-9
- 26 Berk, A.; Bernstein, L.S. & Robertson, D.C. (1989). MODTRAN: A Moderate Resolution
27 Model for LOWTRAN 7, GL-TR-89-0122, Geophys. Lab., Bedford, MA, USA
28 38pp.
- 29 Gascon, F. (2001). Modélisation Physique d'Images de Télédétection Optique. PhD Thesis.
30 Université Paul Sabatier, Toulouse, France.
- 31 Gastellu-Etchegorry, J.P.; Demarez, V.; Pinel V. & Zagolski F. (1996). Modeling radiative
32 transfer in heterogeneous 3-D vegetation canopies, *Remote Sensing of*
33 *Environment*, 58: 131-156.

- 1 Gastellu-Etchegorry, J.P.; Guillevic, P.; Zagolski, F.; Demarez, V.; Trichon, V.; Deering, D. &
2 Leroy, M. (1999). Modeling BRF and radiation regime of tropical and boreal forests
3 - BRF. *Remote Sensing of Environment*, 68: 281-316.
- 4 Gastellu-Etchegorry, J.P.; Martin, E. & Gascon, F. (2004), DART: a 3-D model for simulating
5 satellite images and surface radiation budget, 2004, *International Journal of Remote*
6 *Sensing*, 25 (1): 75-96.
- 7 Gastellu-Etchegorry, J.P. (2008). 3D modeling of satellite spectral images - Radiation budget
8 and energy budget of urban landscapes, *Meteorology and Atmosphere Physics*,
9 Vol. 102, N 3-4, pp187-207
- 10 Gastellu-Etchegorry, J.P.; Grau, E.; Rubio, J.; Ueberschlag, A.; Sun, G.; Brut, A.; Cros, J. &
11 Lauret, N. (2010). 3-D Monte Carlo radiative transfer with DART model - An
12 application to Lidar modeling. Third International Symposium Recent Advances in
13 Quantitative Remote Sensing, 27 September to 1 October 2010. Torrent-Valencia,
14 Spain.
- 15 Govaerts, Y. & Verstraete, M.M. (1998). Raytran: A Monte Carlo ray tracing model to
16 compute light scattering in three-dimensional heterogeneous media. *IEEE*
17 *Transactions on Geoscience and Remote Sensing*, 36, 493-505.
- 18 Grau, E. (2011). Modélisation 3D optique d'images de télédétection et du bilan radiation des
19 paysages terrestres. PhD thesis. Paul Sabatier University.
- 20 Guillevic, P. & Gastellu-Etchegorry, J.P. (1999). Modeling BRF and radiation regime of
21 tropical and boreal forests - PAR regime. *Remote Sensing of Environment*, 68: 317-
22 340.
- 23 Jacquemoud, S. & Baret, F. (1990). PROSPECT: a model of leaf optical properties spectra,
24 *Remote Sensing of Environment*, 34(2):75-91.
- 25 Kimes, D.S. & Sellers, P.J. (1985). Inferring hemispherical reflectance of the Earth's surface
26 for global energy budgets from remotely sensed nadir or directional radiance
27 values. *Remote Sensing of Environment*, 18: 205-223.
- 28 Malenovský, Z.; Martin, E.; Homolová, L.; Gastellu-Etchegorry, J.-P.; Zurita-Milla, R.;
29 Schaepman, M.E.; Pokorný, R.; Clevers, J.G.P.W. & Cudlín, P. (2008). Influence of
30 woody elements of a Norway spruce canopy on nadir reflectance simulated by the
31 DART model at very high spatial resolution. *Remote Sensing of Environment*.
32 112:1-18.
- 33 Malenovský, Z.; Ufer, C.; Lhotakova, Z.; Clevers, J.G.P.W.; Schaepman, M.E.; Albrechtova, J.
34 & Cudlín, P. (2006). A new hyperspectral index for chlorophyll estimation of a
35 forest canopy: Area under curve normalised to maximal band depth between 650-
36 725 nm, *EARSeL eProceedings* 5 (2). p. 161 - 172.
- 37 Malenovský, Z.; Martin, E.; Homolova, L.; Pokorny, R.; Schaepman, M.E.;
38 Gastellu-Etchegorry, J.-P.; Zurita Milla, R.; Clevers, J.G.P.W. & Cudlín, P. (2005).
39 Influence of forest canopy structure simulated using the Discrete Anisotropic
40 Radiative Transfer (DART) model on the retrieval of spruce stand LAI. In:
41 9th International Symposium on Physical Measurements and Signatures in
42 Remote Sensing (ISPMSRS), Beijing, 17-19 October 2005. Beijing: ISPRS WG
43 VII/1, p. 3.

- 1 Martin, E. (2006). DART: Modèle 3D Multispectral et Inversion d'Images Optiques de
2 Satellite - Application aux couverts forestiers. PhD thesis. Paul Sabatier
3 University.
- 4 Masson, V. (2000). A physically-based scheme for the urban energy budget in atmospheric
5 models, *Boundary-layer Meteorology*, 94:357-397.
- 6 Masson, V.; Gomes, L.; Pigeon, G.; Liousse, C.; Pont, V.; Lagouarde, J.-P.; Voogt, J. A.;
7 Salmond, J.; Oke, T. R.; Legain, D.; Garrouste, O.; Lac, C.; Connan, O.; Briottet, X. &
8 Lachéradé, S. (2007). The Canopy and Aerosol Particles Interaction in Toulouse
9 Urban Layer (CAPITOU) experiment. *Meteorology and Atmospheric Physics*,
10 Vol. 102, N 3-4, pp137-157
- 11 North, P.R.J. (1996). Three-dimensional forest light interaction model using a Monte
12 Carlo method, *IEEE Transactions on Geoscience and Remote Sensing*, 34, 946-
13 956.
- 14 Pinel, V. & Gastellu-Etchegorry, J.P. (1998). Sensitivity of Texture of High Resolution Images
15 of Forest to Biophysical and Acquisition Parameters. *Remote Sensing of
16 Environment*. 65: 61-85.
- 17 Pinty, B.; Gobron, N.; Widlowski, J.L.; Gerstl, S.A.W.; Verstraete, M.M.; Antunes, M.; Bacour,
18 C.; Gascon, F.; Gastellu-Etchegorry, J.P.; Jacquemoud, S.; North, P.; Qin, W. &
19 Thompson, R. (2001). Radiation transfer model intercomparaison (RAMI) exercise,
20 *Journal of Geophysical Research*, 106, D11, 11937-11956.
- 21 Pinty, B.; Widlowski, J.-L.; Taberner, M.; Gobron, N.; Verstraete, M. M.; Disney, M.; Gascon,
22 F.; Gastellu-Etchegorry, J.-P.; Jiang, L.; Kuusk, A.; Lewis, P.; Li, X.; Ni-Meister, W.;
23 Nilson, T.; North, P.; Qin, W.; Su, L.; Tang, S.; Thompson, R.; Verhoef, W.; Wang,
24 H.; Wang, J.; Yan, G. & H. Zang (2004). RAdiation transfer Model Intercomparison
25 (RAMI) exercise: Results from the second phase, *Journal of Geophysical Research*,
26 109, D06210 10.1029/2003JD004252.
- 27 Soux, C.A.; Voogt, J.A. & Oke, T.R. (2004). A model to calculate what a remote sensor 'sees'
28 of an urban surface, *Boundary Layer Meteorology*, 111:109-132.
- 29 Thompson, R.L. & Goel, N.S. (1998). Two models for rapidly calculating bidirectional
30 reflectance: Photon spread (ps) model and statistical photon spread (sps) model.
31 *Remote Sensing Reviews*, 16, 157-207.
- 32 Ueberschlag, A. (2010). Etude des couverts forestiers par inversion de formes d'onde Lidar à
33 l'aide du modèle de transfert radiatif DART, *XYZ*, 126: 22-26.
- 34 Voogt, J.A. & Oke, T.R. (1998). Effects of urban surface geometry on remotely sensed surface
35 temperature, *Int. J. Remote Sensing*, 19: 895-920.
- 36 Voogt, J.A. & Oke, T.R. (2003). Thermal remote sensing of urban climates, *Remote Sensing of
37 Environment*, 86:370-384.
- 38 Widlowski, J.L.; Taberner, M.; Pinty, B.; Bruniquel-Pinel, V.; Disney, M.; Fernandes, R.;
39 Gastellu-Etchegorry, J.-P.; Gobron, N.; Kuusk, A.; Lavergne, T.; Leblanc, S.; Lewis,
40 P. E.; Martin, E.; Mottus, M.; North, P. R. J.; Qin, W.; Robustelli, M.; Rochdi, N.;
41 Ruiloba, R.; Soler, C.; Thompson, R.; Verhoef, W.; Verstraete, M.M. & Xie, D. (2007).
42 The third RAdiation transfer Model Intercomparison (RAMI) exercise:
43 Documenting progress in canopy reflectance models, *J. Geophysical Research*, 112,
44 D09111, doi: 10.1029/2006JD007821

- 1 Widlowski, J-L; Robustelli, M.; Disney, M.; Gastellu-Etchegorry, J.-P.; Lavergne, T.; Lewis,
- 2 P.; North, P.R.J.; Pinty, B.; Thompson, R. & Verstraete, M.M. (2008). The RAMI On-
- 3 line Model Checker (ROMC): A web-based benchmarking facility for canopy
- 4 reflectance models, *Remote Sensing of Environment*, 112:1144-1150.